

# Wind nebulae and supernova remnants of very massive stars

D. M.-A. Meyer<sup>\*1</sup>, M. Petrov<sup>2</sup> and M. Pohl<sup>1,3</sup>

<sup>1</sup> *Institut für Physik und Astronomie, Universität Potsdam, Karl-Liebknecht-Strasse 24/25, 14476 Potsdam, Germany*

<sup>2</sup> *Max Planck Computing and Data Facility (MPCDF), Gieenbachstrasse 2, D-85748 Garching, Germany*

<sup>3</sup> *DESY Platanenallee 6, D-15738 Zeuthen, Germany*

Received; accepted

## ABSTRACT

A very small fraction of (runaway) massive stars have masses exceeding  $60\text{--}70 M_{\odot}$  and are predicted to evolve as Luminous-Blue-Variable and Wolf-Rayet stars before ending their lives as core-collapse supernovae. Our 2D axisymmetric hydrodynamical simulations explore how a fast wind ( $2000 \text{ km s}^{-1}$ ) and high mass-loss rate ( $10^{-5} M_{\odot} \text{ yr}^{-1}$ ) can impact the morphology of the circumstellar medium. It is shaped as 100 pc-scale wind nebula which can be pierced by the driving star when it supersonically moves with velocity  $20\text{--}40 \text{ km s}^{-1}$  through the interstellar medium (ISM) in the Galactic plane. The motion of such runaway stars displaces the position of the supernova explosion out of their bow shock nebula, imposing asymmetries to the eventual shock wave expansion and engendering Cygnus-loop-like supernova remnants. We conclude that the size (up to more than 200 pc) of the filamentary wind cavity in which the chemically enriched supernova ejecta expand, mixing efficiently the wind and ISM materials by at least 10% in number density, can be used as a tracer of the runaway nature of the very massive progenitors of such 0.1 Myr old remnants. Our results motivate further observational campaigns devoted to the bow shock of the very massive stars BD+43 3654 and to the close surroundings of the synchrotron-emitting Wolf-Rayet shell G2.4+1.4.

**Key words:** methods: numerical – shock waves – stars: circumstellar matter – stars: massive.

## 1 INTRODUCTION

Massive stars ( $M_{*} \geq 8 M_{\odot}$ ) are objects whose formation is an uncommon but crucial event in the interstellar medium (ISM) of our Galaxy (Langer 2012). Their strong winds release a large amount of momentum and energy into their surrounding ISM and form bubbly circumstellar structures which chemically enrich their local environment (Weaver et al. 1977). Wind bubbles of main-sequence, OB-type massive stars are predicted to expand up to  $\simeq 100$  pc away from the star. The shocked photoionised stellar wind material and the ISM gas are separated by an unstable contact discontinuity segregating the inner hot, diluted shocked wind gas from the outer layer of cold, dense shocked ISM gas. These nebulae grow inside the huge H II regions generated by the ionising radiation field of early-type hot massive stars (Dyson 1975; Dyson & Gulliford 1975), however, sufficiently massive stellar wind bubbles can trap the ionisation front of their own central star (Dwarkadas & Rosenberg 2013). Wind bubbles mainly radiate by means of optical forbidden-line emission (Schneps et al. 1981; Smith et al. 1984), in the X-ray energy band via thermal photons emitted by the inner hot region (Zhekov 2014), and in the infrared waveband by reprocessing of starlight by ISM dust that is trapped into the outer layer of the bubble (van Buren & McCray 1988). Stellar wind bubbles

of static massive stars conserve their spherical shape regardless of the central star’s evolution, see Garcia-Segura et al. (1996); Freyer et al. (2003, 2006); Dwarkadas (2007).

The spherical symmetry of stellar wind nebulae is broken if their central star moves with respect to their local ambient medium, and they eventually turn into a similarly organised but arc-like shape (Baranov et al. 1971; Wilkin 1996). The resulting so-called stellar wind bow shocks form around the 4 to 10 per cent of all main-sequence stars that move supersonically through the ISM (see Gies 1987; Blaauw 1993; Huthoff & Kaper 2002). The physics of bow shocks around OB stars partly relies of the (in)efficiency of heat conduction (Meyer et al. 2017; Green et al. 2019) while their detailed internal structure depends on the coupling between dust and gas (Henney & Arthur 2019a,b,c). Their morphology is a function of the stellar mass-loss rate (Gull & Sofia 1979; Gvaramadze et al. 2014; Meyer et al. 2014), ambient medium density (Kaper et al. 1997), and stellar bulk motion (Meyer et al. 2014), respectively. The evolution of massive stars induces brutal changes in the stellar wind properties (Langer 2012). The dense but slow wind of evolved red supergiant stars makes bow shocks prone to develop thin-shell instabilities (Dgani et al. 1996; Blondin & Koerwer 1998; Mackey et al. 2012; Meyer et al. 2014), which can be inhibited either by an external ionising radiation field (Meyer et al. 2014) or by the ambient magnetisation of the ISM (van Marle et al. 2014). These dusty nebulae are mainly observable in the infrared wave-

\* E-mail: dmameyer.astro@gmail.com

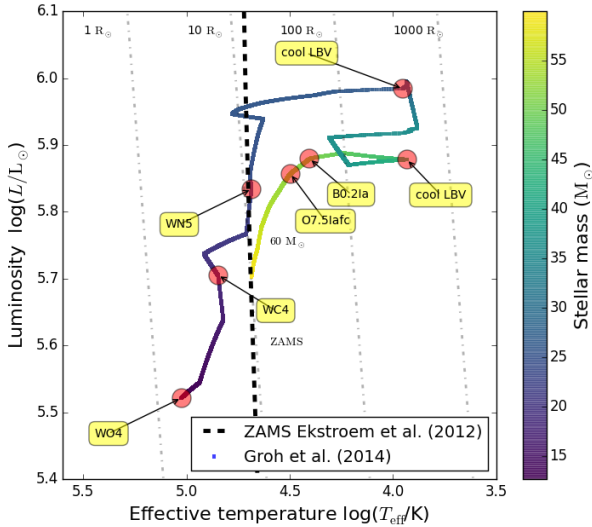


**Figure 1.** Hertzsprung-Russell diagram of the non-rotating  $60 M_{\odot}$  zero-age-main-sequence (ZAMS) star considered in this study, based on Groh et al. (2014).

band (van Buren 1993; van Buren et al. 1995; van Marle et al. 2011; Cox et al. 2012; Peri et al. 2012; Mackey et al. 2014; Peri et al. 2015; Kobulnicky et al. 2016, 2017, 2018) although they thermally emit in the other wavebands, see Kaper et al. (1997); Jorissen et al. (2011). Interestingly, such bow shocks are suspected to accelerate protons and electrons in the stellar wind to high energies and to act as cosmic ray injectors (del Valle et al. 2013, 2015; del Valle & Pohl 2018), producing variable high-energy and  $\gamma$ -ray emission (del Valle & Romero 2014), however at much lower luminosity than, e.g. pulsars or supernova remnants (De Becker et al. 2017; Toalá et al. 2017; Binder et al. 2019). Recent measures have reported synchrotron emission from the Wolf-Rayet ring bubble G2.4+1.4 (Prajapati et al. 2019).

When bow-shock-driving massive stars cease to evolve, the distorted bubble nebula shaped throughout the post-ZAMS (zero-age-main-sequence) star life constitutes the environment in which the moving high-mass star dies, e.g. as a core-collapse supernova (Franco et al. 1991; Rozyczka et al. 1993; Ekström et al. 2012). The deviations from the spherically-symmetric expansion of the shock wave depend on the density and mass accumulated in the circumstellar medium of the progenitor. The blastwave first expands in a cavity of unshocked stellar wind, before interacting with the reverse shock of the bow shock, whose presence slows down the progression of the shock wave in the direction of motion of the progenitor, while it facilitates its rapid expansion in the opposite direction, inducing characteristic asymmetries in the supernova remnant. Typical examples among young supernova remnants are Kepler’s supernova remnant (Borkowski et al. 1992; Velázquez et al. 2006; Chiotellis et al. 2012), Tycho (Vigh et al. 2011; Williams et al. 2013), or the Cygnus Loop (Meyer et al. 2015; Fang et al. 2017). Note that asymmetries can be caused by the geometry of the explosion itself (Toledo-Roy et al. 2014). Having established that the morphology of supernova remnants from massive progenitors is a function of their past stellar evolution, the question arises, which massive stars are most prone to generate a dense asymmetric circumstellar medium and hence the most aspherical remnants?

The accumulation of mass in the surroundings of an evolving star can arise from the brutal release of dense shells of material

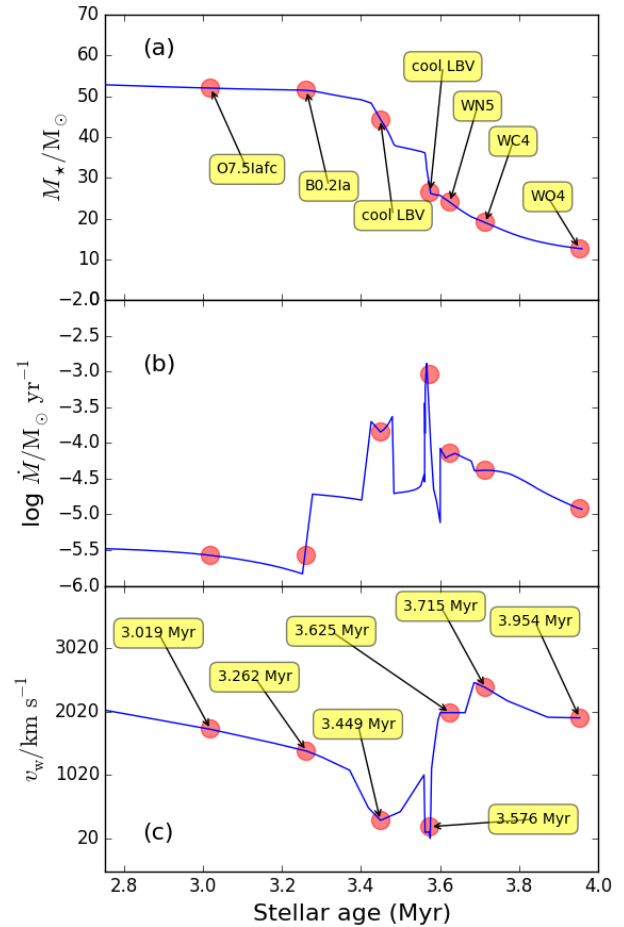


**Figure 2.** Post-main-sequence evolution of the stellar mass (top, panel a), mass-loss rate (middle, panel b), and wind velocity (bottom, panel c) as a function of time (in Myr), that we used as initial condition in our hydrodynamical simulations.

during the post-main-sequence phase. As additional effect to that of the progenitor’s stellar motion, this naturally leads to asymmetric and inhomogeneous cavities in which the supernova blastwave will expand. This particularly affects high-mass stars evolving through eruptive stellar evolutionary stages such as so-called luminous blue variable or Wolf-Rayet phases (González & Koenigsberger 2014; Humphreys et al. 2017), characterised by the sudden inflation of the star together with an increase of the star’s mass-loss rate and wind velocity. This results in the ejection of dense shells of envelope material into the stellar surroundings (Sanyal et al. 2017; Gräfener et al. 2017; Grassitelli et al. 2018). Such evolving high-mass stars, that are rare and predicted to end their life as a core-collapse supernova (Meynet & Maeder 2005; Ekström et al. 2012), have been observed both in the Milky Way (van der Hucht 2001) and in the Large Magellanic Cloud (Hainich et al. 2014). Moreover, a significant fraction of them have fast proper motion, which can be explained by many-body gravitational interaction leading to their escape from their parent cluster (Gvaramadze & Gualandris 2011; Gvaramadze et al. 2013). Particularly, this mechanism is able to produce very massive ( $\simeq 55$ - $85 M_{\odot}$ ) fast-moving stars such as the main-sequence star BD+43°3654 which runs away from the Cygnus OB2 region (Comerón & Pasquali 2007). Hence, these moving stellar objects that are inclined to provoke morphologi-

**Table 1.** Simulation models in this study. The table gives the space velocity of the moving star,  $v_*$ . The runs are labelled as “CSM” for the pre-supernova modelling of the circumstellar medium and as “SNR” for the simulations of their subsequent remnants, respectively.

Model	$v_*$ (km s <sup>-1</sup> )	Grid size	Grid mesh	description
Run-0-CSM	0	[0; 150] × [−150; 150]	3000 × 6000 cells	static wind bubble
Run-10-CSM	10	[0; 150] × [−200; 100]	2000 × 4000 cells	wind bubble with off-centered slowly-moving star
Run-20-CSM	20	[0; 175] × [−250; 100]	2000 × 4000 cells	bow shock of runaway star moving with Mach number $M = 1^a$
Run-40-CSM	40	[0; 150] × [−300; 100]	1500 × 4000 cells	bow shock of runaway star moving with Mach number $M = 2^a$
Run-0-SNR	0	[0; 200] × [−200; 200]	3500 × 7000 cells	supernova remnant of static progenitor
Run-10-SNR	10	[0; 200] × [−230; 170]	4000 × 8000 cells	supernova remnant of slowly-moving progenitor
Run-20-SNR	20	[0; 200] × [−275; 175]	3200 × 7000 cells	supernova remnant of progenitor moving with Mach number $M = 1^a$
Run-40-SNR	40	[0; 200] × [−330; 170]	3200 × 8000 cells	supernova remnant of progenitor moving with Mach number $M = 2^a$

(a) The stellar motion is supersonic with respect to the unperturbed ISM sound speed.

cal distortions of their wind nebulae O’Hara et al. (2003) are also good candidates for the production of strongly asymmetric supernova remnants. In this study, we explore the effects of consecutive luminous blue variable and Wolf-Rayet winds onto the shaping of nebulae around a 60  $M_\odot$  star (Freyer et al. 2003; van Marle et al. 2007; Toalá & Arthur 2011; Wareing et al. 2017) (see Fig. 1), and we investigate how its bulk motion can affect the development of asymmetries in their subsequent supernova remnant in the spirit of the first paper of this series devoted to runaway red supergiant progenitors (Meyer et al. 2015).

Our study is divided as follows. First, we present in Section 2 the methods for the numerical modelling of the circumstellar medium of a moving, massive Wolf-Rayet-evolving star. We present our results for the dynamics of the stellar surroundings from the ZAMS to the supernova remnant phase in Section 3. Particularly, we concentrate on the mixing of material induced in the remnants and on their associated thermal X-ray emission properties. Our outcomes are further discussed in Section 4. Finally, we conclude in Section 5.

## 2 METHOD

This section introduces the reader to the methods used to perform hydrodynamical simulations of the surroundings of a massive star undergoing both luminous blue variable and Wolf-Rayet phases. The evolution of the circumstellar medium is simulated from the zero-age main sequence of the progenitor to the late phase of supernova remnant evolution, for several proper-motion speeds of the driving star.

### 2.1 Simulation method for the pre-supernova phase

The structure of the pre-supernova circumstellar medium arises from stellar wind-ISM interaction. We model it with the same method as was used for studying bow shocks of runaway massive stars, summarised in Meyer et al. (2016). The stellar surroundings are simulated with axisymmetric, two-dimensional numerical hydrodynamics simulations performed with the PLUTO<sup>1</sup> code (Mignone et al. 2007, 2012). We use cylindrical coordinates with a uniform grid  $[O; R_{\max}] \times [z_{\min}; z_{\max}]$  that is discretised with  $N_R \times N_z$  grid zones. The uniform spatial mesh resolution is  $\Delta = R_{\max}/N_R = (z_{\max} - z_{\min})/N_z$ . The supersonic stellar wind is injected into the computational domain via a sphere of 20 cells

in radius centered at the origin of the grid and filled with the wind density profile,

$$\rho_w = \frac{\dot{M}}{4\pi r^2 v_w}, \quad (1)$$

where  $\dot{M}$  denotes the time-dependent mass-loss rate of the massive star,  $r$  is the distance to the origin of the domain,  $O$ , and  $v_w$  is the wind velocity. The same method has been used in Comerón & Kaper (1998) and van Marle et al. (2007, 2011, 2014). The stellar wind parameters  $\rho_w$  and  $v_w$  are time-dependently interpolated from the tabulated stellar evolution model of a non-rotating 60  $M_\odot$  star presented in Groh et al. (2014). The wind-blown bubble resulting from the wind-ISM interaction is computed in the rest frame of the central star, and its proper stellar motion  $v_*$  is taken into account by setting an inflowing medium at the  $z = z_{\max}$  boundary. Outflow boundary conditions are assigned at  $z = z_{\min}$  and  $R = R_{\max}$ , respectively. The stellar wind material injected into the domain is distinguished from the ambient medium using a passive tracer,  $Q_1$ , that is initially set to  $Q_1(\mathbf{r}) = 1$  in the wind material and to  $Q_1(\mathbf{r}) = 0$  in the ISM gas, respectively. We follow the mixing of materials in the circumstellar structure using the advection equation,

$$\frac{\partial(\rho Q_1)}{\partial t} + \nabla \cdot (\mathbf{v} \rho Q_1) = 0. \quad (2)$$

The computationally-intensive calculations were performed on the HPC systems Cobra using Intel Skylake processors and Draco using Intel Haswell, Broadwell processors at the Max Planck Computing and Data Facility (MPCDF<sup>2</sup>) in Garching, and on the North-German Supercomputing Alliance (HLRN<sup>3</sup>) using the HPC compute system in Berlin operating with Cray XC40/30 processors, respectively.

### 2.2 Setting up the supernova explosion

Once the pre-supernova circumstellar medium has been modelled, we insert a spherically-symmetric explosion into a spherically-symmetric stellar wind in order to separately calculate in 1D fashion the initial expansion of the supernova shock wave into the progenitor’s last freely-expanding wind, whose solution is used as initial condition for the 2D supernova remnants (Meyer et al. 2015). The expanding blastwave is characterized by its energy, taken to be  $E_{\text{ej}} = 10^{51}$  erg, and by the mass of the ejecta released at the time

<sup>1</sup> <http://plutocode.ph.unito.it/>

<sup>2</sup> <https://www.mpcdf.mpg.de/>

<sup>3</sup> <https://www.hlrn.de/>

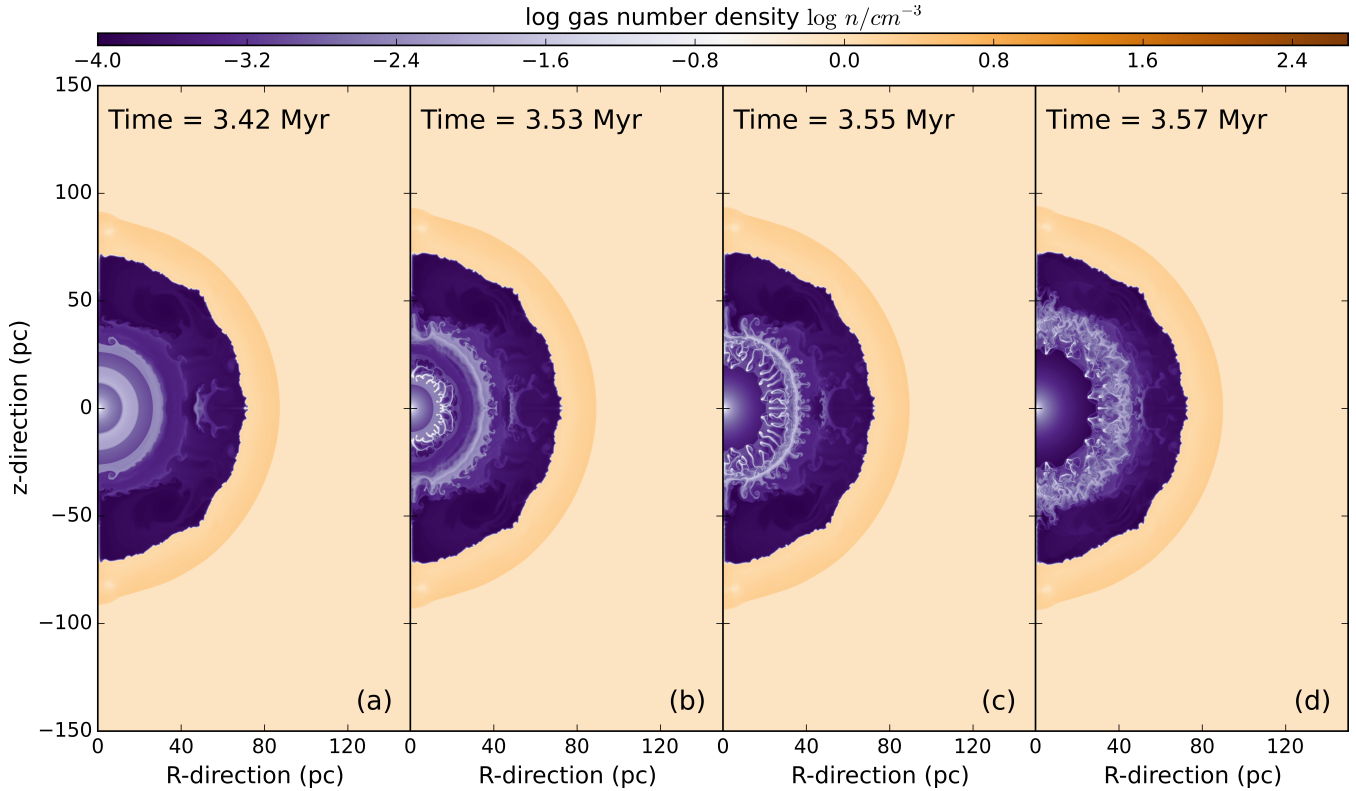


**Figure 3.** Time sequence of density maps (in  $\text{cm}^{-3}$ ) with circumstellar shells released inside the stellar wind bubble generated by our massive star at rest ( $v_* = 0 \text{ km s}^{-1}$ ), while it passes through two successive luminous-blue-variable phases before the Wolf-Rayet wind blows. The panels are shown at times 3.42 (a), 3.53 (b), 3.55 (c) and 3.57 Myr (d), respectively. On each panel the star is located at the origin.

of the explosion,  $M_{\text{ej}}$ , estimated as

$$M_{\text{ej}} = M_* - \int_{t_{\text{ZAMS}}}^{t_{\text{SN}}} \dot{M}(t) dt - M_{\text{NS}} = 11.1 M_{\odot}, \quad (3)$$

where  $t_{\text{ZAMS}}$  and  $t_{\text{SN}}$  are the zero-age-main-sequence and supernova times, respectively, and where  $M_{\text{NS}} = 1.4 M_{\odot}$  is the mass of the remnant neutron star.

The expansion of the supernova shock wave is launched using the method of Whalen et al. (2008) and van Veelen et al. (2009), in which a blastwave density profile,  $\rho(r)$ , is deposited on the top of the progenitor's wind profile taken from the modelled nebulae, at the pre-supernova time. We ensure that the outer boundary of this 1D computational domain is smaller than the value of the wind termination shock of the pre-shaped circumstellar medium. The ejecta profile is defined by two characteristic lengths corresponding to the radius of the progenitor's core at the moment of the explosion,  $r_{\text{core}}$ , and the position of the forward shock of the blastwave,  $r_{\text{max}}$ . The simulation is initialised at time  $t_{\text{max}} = r_{\text{max}}/v_{\text{max}}$ , with  $v_{\text{max}} = 30000 \text{ km s}^{-1}$  the ejecta top speed (van Veelen et al. 2009). The quantity  $r_{\text{max}}$  is a free parameter determined according to the numerical procedure described in Whalen et al. (2008). The density profile of the ejecta follows a piece-wise function,

$$\rho(r) = \begin{cases} \rho_{\text{core}}(r) & \text{if } r \leq r_{\text{core}}, \\ \rho_{\text{max}}(r) & \text{if } r_{\text{core}} < r < r_{\text{max}}, \\ \rho_{\text{csm}}(r) & \text{if } r \geq r_{\text{max}}, \end{cases} \quad (4)$$

with a constant density,

$$\rho_{\text{core}}(r) = \frac{1}{4\pi n} \frac{(10E_{\text{ej}}^{n-5})^{-3/2}}{(3M_{\text{ej}}^{n-3})^{-5/2}} \frac{1}{t_{\text{max}}^3}, \quad (5)$$

imposed for the plateau of the ejecta in the  $[0; r_{\text{core}}]$  region of the domain. The quantity

$$\rho_{\text{max}}(r) = \frac{1}{4\pi n} \frac{(10E_{\text{ej}}^{n-5})^{(n-3)/2}}{(3M_{\text{ej}}^{n-3})^{(n-5)/2}} \left(\frac{r}{t_{\text{max}}}\right)^{-n}, \quad (6)$$

is a function of  $r_{\text{core}}$  and  $r_{\text{max}}$  (Truelove & McKee 1999), where the index,  $n$ , is set to  $n = 11$  that is typical for core-collapse supernova explosions (Chevalier 1982). In Eqs. (4),  $\rho_{\text{csm}}$  is the freely-expanding wind profile measured from the pre-supernova simulations of the circumstellar medium. The ejecta speed follows a homologous-expansion profile,

$$v(r) = \frac{r}{t}, \quad (7)$$

for times  $t > t_{\text{max}}$ , where  $t$  is the time after the supernova explosion. The velocity of the ejecta at the location of  $r_{\text{core}}$  reads,

$$v_{\text{core}} = \left(\frac{10(n-5)E_{\text{ej}}}{3(n-3)M_{\text{ej}}}\right)^{1/2}, \quad (8)$$

see Truelove & McKee (1999). The 1D solution for the ejecta-wind interaction is mapped onto the 2D domain when the forward shock of the expanding supernova blastwave reaches 8 pc. With the grid resolution that we consider, the mapped ejecta profiles are hence resolved with  $\sim 160$  grid zones.

Last, a second passive scalar  $Q_2(r)$  is introduced, obeying the

advection equation

$$\frac{\partial(\rho Q_2)}{\partial t} + \nabla \cdot (\mathbf{v}\rho Q_2) = 0, \quad (9)$$

which distinguishes the ejecta from the stellar wind and the ambient medium materials. It is initially set to  $Q_2(\mathbf{r}) = 1$  for the region made of supernova ejecta material and to  $Q_2(\mathbf{r}) = 0$  in the other part of the computational domain, respectively.

### 2.3 Governing equations

We model the stellar wind-ISM interaction and the supernova remnant within the framework of the non-ideal hydrodynamics, i.e. by solving the Euler equations and by accounting for energy losses by optically-thin radiative cooling. We solve the set of equations composed of the equation for the conservation of mass,

$$\frac{\partial \rho}{\partial t} + \nabla \cdot (\rho \mathbf{v}) = 0, \quad (10)$$

of linear momentum,

$$\frac{\partial \rho \mathbf{v}}{\partial t} + \nabla \cdot (\mathbf{v} \otimes \rho \mathbf{v}) + \nabla p = 0, \quad (11)$$

and of the total energy,

$$\frac{\partial E}{\partial t} + \nabla \cdot (E \mathbf{v}) + \nabla \cdot (p \mathbf{v}) = \Phi(T, \rho), \quad (12)$$

where

$$E = \frac{p}{(\gamma - 1)} + \frac{\rho v^2}{2}, \quad (13)$$

and  $\rho$  is the mass density of the gas,  $p$  its pressure,  $\mathbf{v}$  the vector velocity, respectively. The gas temperature reads,

$$T = \mu \frac{m_{\text{H}}}{k_{\text{B}}} \frac{p}{\rho}, \quad (14)$$

where  $k_{\text{B}}$  is the Boltzmann constant and  $\mu$  is the mean molecular weight, so that the gas mass density reads,

$$\rho = \mu n m_{\text{H}}, \quad (15)$$

with  $n$  the total number density of the plasma and  $m_{\text{H}}$  the mass of a hydrogen atom. The adiabatic index of the gas is set to  $\gamma = 5/3$ . As in Meyer et al. (2015), we use a finite-volume method with the Harten-Lax-van Leer approximate Riemann solver, and integrate the Euler equations with a second order, unsplit, time-marching algorithm.

Our simulations take into account internal energy losses and gains by optically-thin cooling and heating, respectively. These mechanisms are represented with the right-hand term of Eq. (12),

$$\Phi(T, \rho) = n_{\text{H}} \Gamma(T) - n_{\text{H}}^2 \Lambda(T), \quad (16)$$

where  $\Gamma(T)$  and  $\Lambda(T)$  are the heating and cooling components of the expression, respectively, and where  $n_{\text{H}}$  is the hydrogen number density. The contribution for heating,  $\Gamma$ , mimics the reionisation of recombining hydrogen atoms by the photon field of the hot star (Osterbrock & Bochkarev 1989; Hummer 1994). The cooling term is based on the prescriptions by optically-thin cooling derived by Wiersma et al. (2009), accounting for the radiation losses for hydrogen and helium at  $T < 10^6$  K and for metals at  $T \geq 10^6$  K (Wiersma et al. 2009). The cooling curve has been updated with collisionally excited forbidden lines such as [OIII]  $\lambda$  5007 line emission (Henney et al. 2009).

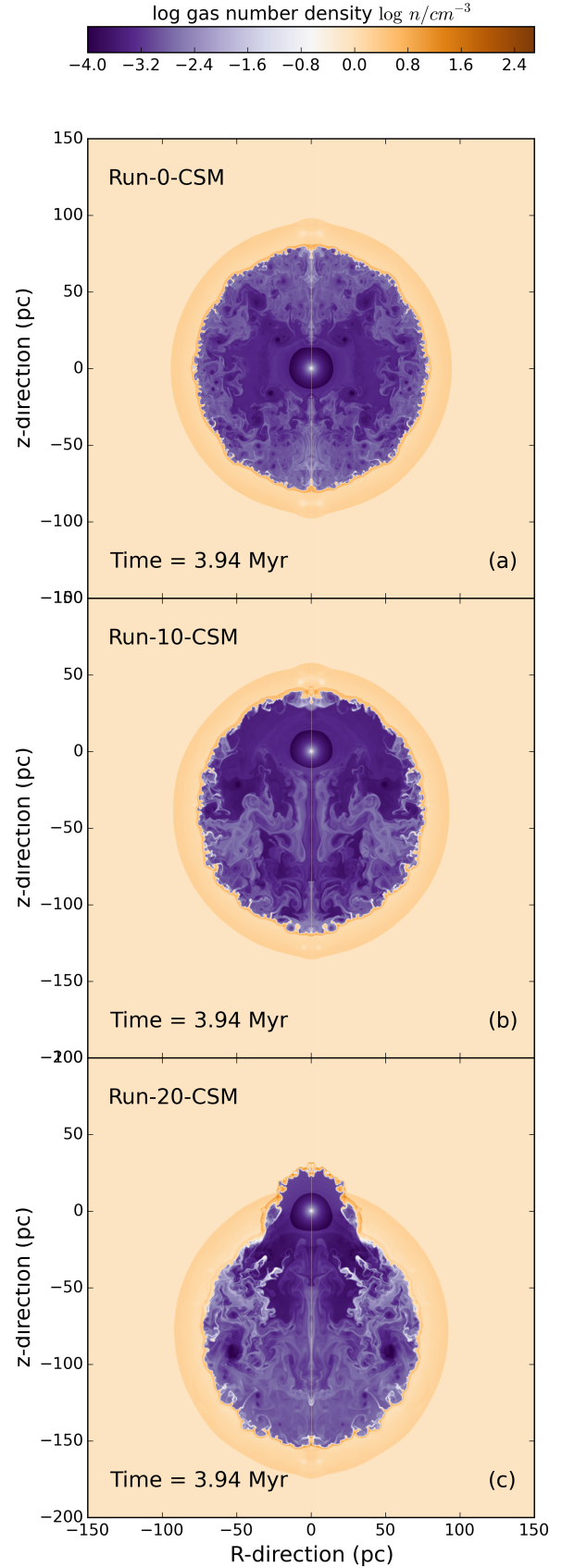


**Figure 4.** Density field (in  $\text{cm}^{-3}$ ) of the circumstellar medium of a massive star moving with  $v_* = 0$  (a), 10 (b), and 20  $\text{km s}^{-1}$  (c) at the pre-supernova time. On each panel the star is located at the origin.

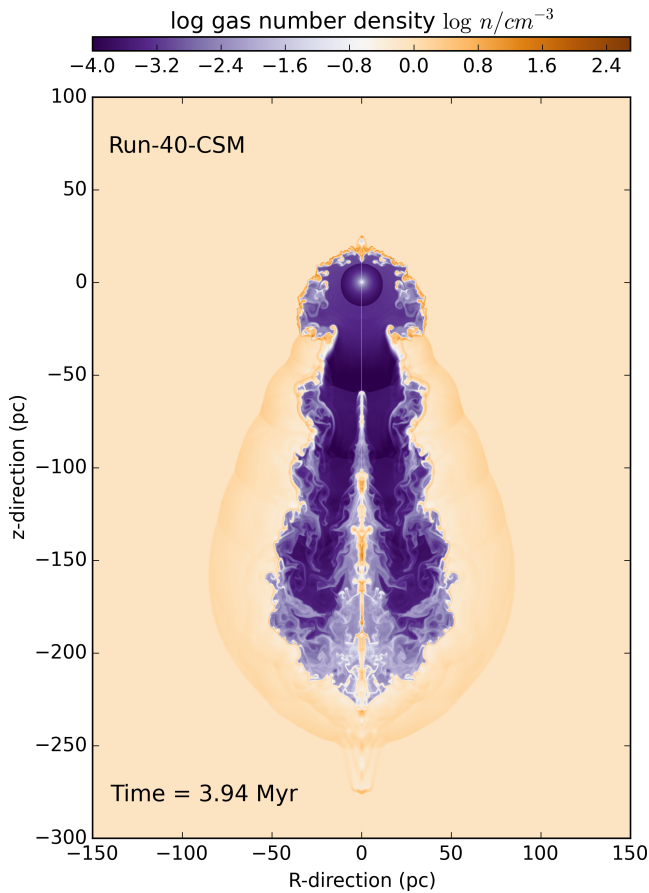


**Figure 5.** Same as Fig. 4 for a star moving with  $v_* = 40 \text{ km s}^{-1}$ . The star is located at the origin.

#### 2.4 Simulation parameters

Fig. 2 plots the stellar surface properties that are used as boundary conditions in our hydrodynamical simulations. The star’s post-main-sequence mass history (panel a, in  $M_\odot$ ), mass-loss rate evolution (panel b, in  $M_\odot \text{ yr}^{-1}$ ), and wind velocity (panel c, in  $\text{km s}^{-1}$ ) are plotted as a function of time (in Myr) starting from 3 Myr. Earlier times correspond to the O-type main-sequence phase of the star during which the stellar wind properties do not evolve much. The red dots on the figures denote the principal evolutionary phases and the yellow labels on the figures indicate the corresponding spectral type. The stellar evolution model of this zero-age-main-sequence non-rotating  $60 M_\odot$  star has been computed up to the Si burning phase with the GENEC code (Ekström et al. 2012). The effective temperature and the terminal wind velocity have been estimated using atmospheric radiative transfer modelling and prescriptions derived from observations of stellar populations (Groh et al. 2014). They are characterised by a long main-sequence phase lasting approximately 3 Myr during which the star blows winds of  $\dot{M} \approx 10^{-6} - 10^{-5.5} M_\odot \text{ yr}^{-1}$ ,  $v_w \approx 3500 - 2000 \text{ km s}^{-1}$  and loses roughly  $8 M_\odot$  of material. Beginning of the last Myr, the mass-loss increases to  $\dot{M} \approx 10^{-5} M_\odot \text{ yr}^{-1}$ , while  $v_w \approx 1300 \text{ km s}^{-1}$ , and the star adopts a B spectral type. This is followed by two consecutive luminous-blue-variable eruptions with  $\dot{M} \approx 10^{-3.5} - 10^{-3} M_\odot \text{ yr}^{-1}$  with wind velocity decreasing down to nearly  $200 \text{ km s}^{-1}$ . The star then evolves to the so-called Wolf-Rayet phase of both high mass-loss rate and a large wind velocity. We do not consider the last pre-supernova increase of the

stellar wind velocity up to  $\approx 5000 \text{ km s}^{-1}$  in this study, as very few examples of such strong-winded Wolf-Rayet stars have been so far monitored (Nugis & Lamers 2000; Toalá et al. 2015).

The free parameter in our series of 2D computationally-intensive simulations is the space velocity of the star,  $v_*$ , which spans from the static case producing a spherical wind-blown bubble ( $v_* = 0 \text{ km s}^{-1}$ ) to the runaway case generating an bow shock ( $v_* = 40 \text{ km s}^{-1}$ ). In all our models, as in the series of papers devoted to a grid of bow shocks models of Meyer et al. (2014, 2016), the massive star is assumed to be located in the warm phase of the ISM, characterised by a temperature of  $8000 \text{ K}$  and a number density of  $0.79 \text{ cm}^{-3}$ . After the modelling of the circumstellar medium of the evolving massive star up the pre-supernova phase, the solution is mapped onto a larger computational domain that is filled with unperturbed ambient ISM material. The supernova explosion is setup according to the method developed in Meyer et al. (2015) and described in the paragraphs above. Our simulation runs and their characteristics are summarised in Table 1.

### 3 RESULTS

In this section, we describe the pre-supernova circumstellar evolution of our  $60 M_\odot$  star and how the expanding supernova blast wave interacts with it. We present the thermal X-ray signatures of the supernova remnants and analyse the mixing of stellar wind, ISM material, and supernova ejecta.

#### 3.1 The pre-supernova circumstellar medium

Our model Run-0-CSM for a static massive star develops a spherical wind bubble of swept-up wind and ISM gas. As the wind properties do not evolve much during the main-sequence phase (Groh et al. 2014), the bubble nebula grows according to the picture described in Weaver et al. (1977). When the OB-type star further evolves, the successive changes in the stellar properties produce several shells that expand at different velocities and eventually collide. Fig. 3 presents the bubble density field of Run-0-CSM for different time instances: at time 3.42 Myr the main-sequence bubble is constituted of an outer dense cold shell of radius around  $60 \text{ pc}$  surrounding a hot diluted region at radii  $25 - 50 \text{ pc}$ , inside of which the post-main-sequence shells are released (Fig. 3a). The dense shells collide with each other (Fig. 3b) and then develop instabilities (Fig. 3c,d) as described in Garcia-Segura et al. (1996); van Marle et al. (2007); van Marle & Keppens (2012). At the pre-supernova time, the circumstellar medium has adopted the shape of a spherically-symmetric structure in which the expanding shells have reached the contact discontinuity of the main-sequence bubble separating hot shocked wind and cold shocked ISM (Fig. 4a). The slow stellar motion of  $10 \text{ km s}^{-1}$  in Run-10-CSM is not sufficient to break this spherical symmetry (Fig. 4b). When the star moves into its own wind bubble, the post-main-sequence shells are released from an off-center location in the bubble. The shell of colliding winds interact first with the bubble in the direction of motion of the star. This rapidly destabilises the contact discontinuity of the nebula ahead of the star’s direction of motion, whereas in the opposite direction the post-main-sequence material interacts later, as a natural consequence of the off-centered position of the star in the nebula (Fig. 4b).

Fig. 4c reports the pre-supernova circumstellar medium in our model Run-20-CSM in which the star moves through the ISM with Mach number  $M = v_*/c_s = 1$ . The main-sequence stellar-wind

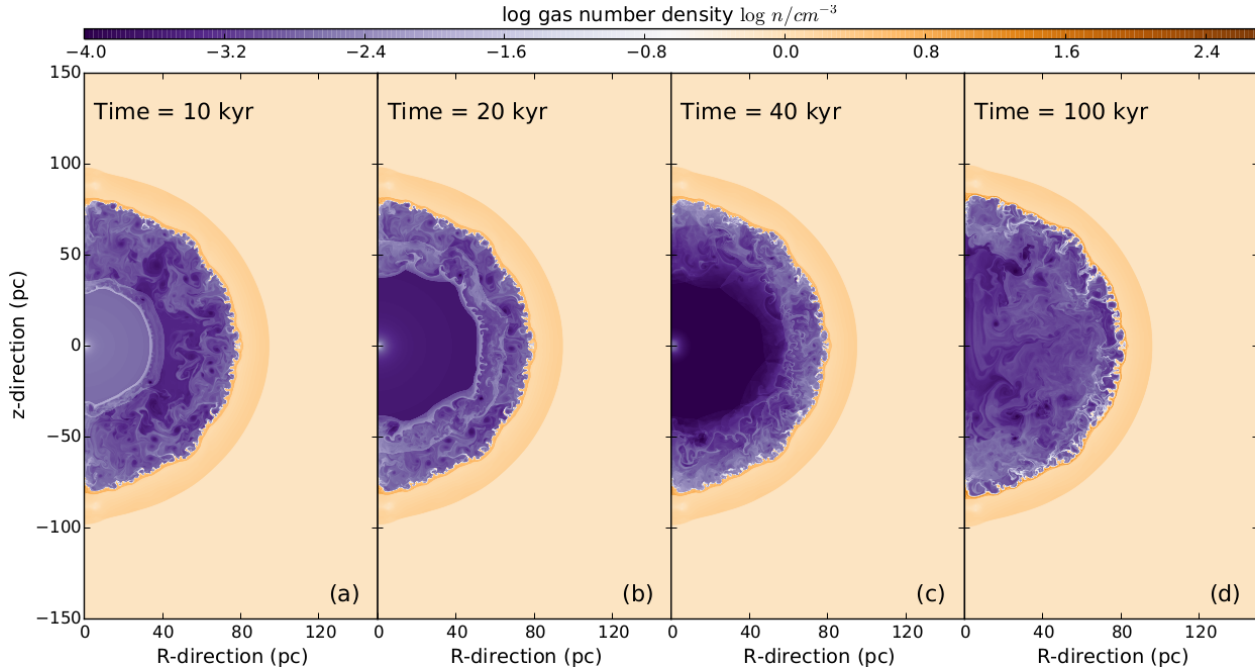


**Figure 6.** Density fields (in  $\text{cm}^{-3}$ ) in the supernova remnant of a  $60 M_{\odot}$  star at rest throughout its entire pre-supernova evolution. Panel a) (left) shows the reflection of the shock wave off the perimeter of the wind bubble at time 10 kyr, and panel b) (right) displays the endstate after internal reflection at time 100 kyr.

bubble is still spherical, and of size similar to that in Run-10-CSM. The star has traveled  $3 \text{ Myr} \times 20 \text{ km s}^{-1} \simeq 60 \text{ pc}$  during its main-sequence phase, which is approximately the final radius of its own wind bubble. The shells of luminous-blue-variable and Wolf-Rayet material are hence released directly in the dense cold shocked ISM gas, not in the stellar wind cavity (Fig. 4a,b). The shells expand freely in the unperturbed ISM ahead of the direction of stellar motion and develop Rayleigh-Taylor instabilities, whereas they fill the interior of the main-sequence wind bubble in the opposite direction. The overall shape of the circumstellar medium therefore becomes strongly asymmetric, i.e. it is shaped as a bubble of cold OB gas with embedded enriched post-main-sequence material, ahead of which a bow shock of thin, unstable but dense material forms into the ambient medium, as a consequence of the high Wolf-Rayet wind density ( $\dot{M} \approx 10^{-5} M_{\odot} \text{ yr}^{-1}$ ). When the star moves even faster, e.g. with velocity  $v_{\star} = 40 \text{ km s}^{-1}$ , the luminous blue variable and Wolf-Rayet shells are expelled out of the main-sequence nebula and expand quasi-spherically into the ISM, see model Run-40-CSM (Fig. 5). The pre-supernova circumstellar medium is completely asymmetric, and only a narrow region of the post-main-sequence ring is connected to the drop-like nebula that reflects the distortion of the wind bubble by the stellar motion. Note that a boundary effect develops as material accumulates close to the symmetry axis (Figs. 4, 5). This well-known problem (Mackey et al. 2015) is unavoidable in two-dimensional axisymmetric simulations of this kind using uniform grids. It can be circumvented by means of three-dimensional calculations, however at the cost of losses in spatial resolution (Rodríguez-González et al. 2019).

### 3.2 Dynamics of asymmetric supernova remnants

If one neglects asymmetries potentially developing in the supernova explosion itself (Toledo-Roy et al. 2014), the remnant of a massive progenitor star at rest conserves its sphericity as the for-

ward shock wave expands symmetrically into the wind cavity. At time 10 kyr it interacts with the dense region of the progenitor’s wind bubble (Fig. 6a) and is reverberated towards the center of the explosion. Subsequent multiple internal reflections of the shock wave generate a large turbulent region (Fig. 6b). In Fig. 7 we show time sequences of the density field (rows) of a supernova remnant produced by a  $60 M_{\odot}$  star moving with different space velocities (columns). The bulk motion of the star spans from  $v_{\star} = 10$  (left column) to  $40 \text{ km s}^{-1}$  (right column), and the remnants are displayed from 10 kyr (top row) up to 100 kyr (bottom row) after the explosion.

Our model Run-10-SNR with a slowly-moving star is plotted in the first column of panels of Fig. 7. The shock wave is clearly identifiable in Fig. 7a as it has not yet interacted with the termination shock of the wind bubble. Reflected shocks forms when the shock wave collides with termination shock of the wind bubble and with the dense main-sequence shell, respectively, making interior of the bubble asymmetric (Fig. 7d). At later times (50-100 kyr), the part of the shock wave which propagates along the stellar direction of motion through the bubble, penetrates the dense layer of shock ISM gas and makes it slightly denser as it had more time to interact with it, while the interior of the remnant is filled with a mixture of low-density, high-temperature ejecta and filamentary shocked wind material which keeps on melting with each other (Fig. 7g,j).

In our model Run-20-SNR the ejecta first fill the protuberance generated by the evolved Wolf-Rayet wind (Fig. 7b). As for a slower supernova progenitor, the shock wave progressively penetrates and expands into the entire upper cavity of the remnant which turns into a hot region of mixed wind and ISM material. The shock wave moves back and forth inside the post-main-sequence mushroom as it experiences multiple reflections between the center of the explosion and the walls of the protuberance (Fig. 7e,h). Once it goes through, a transmitted shock front freely expands into the unperturbed ISM and begins to locally recovers a global spheri-

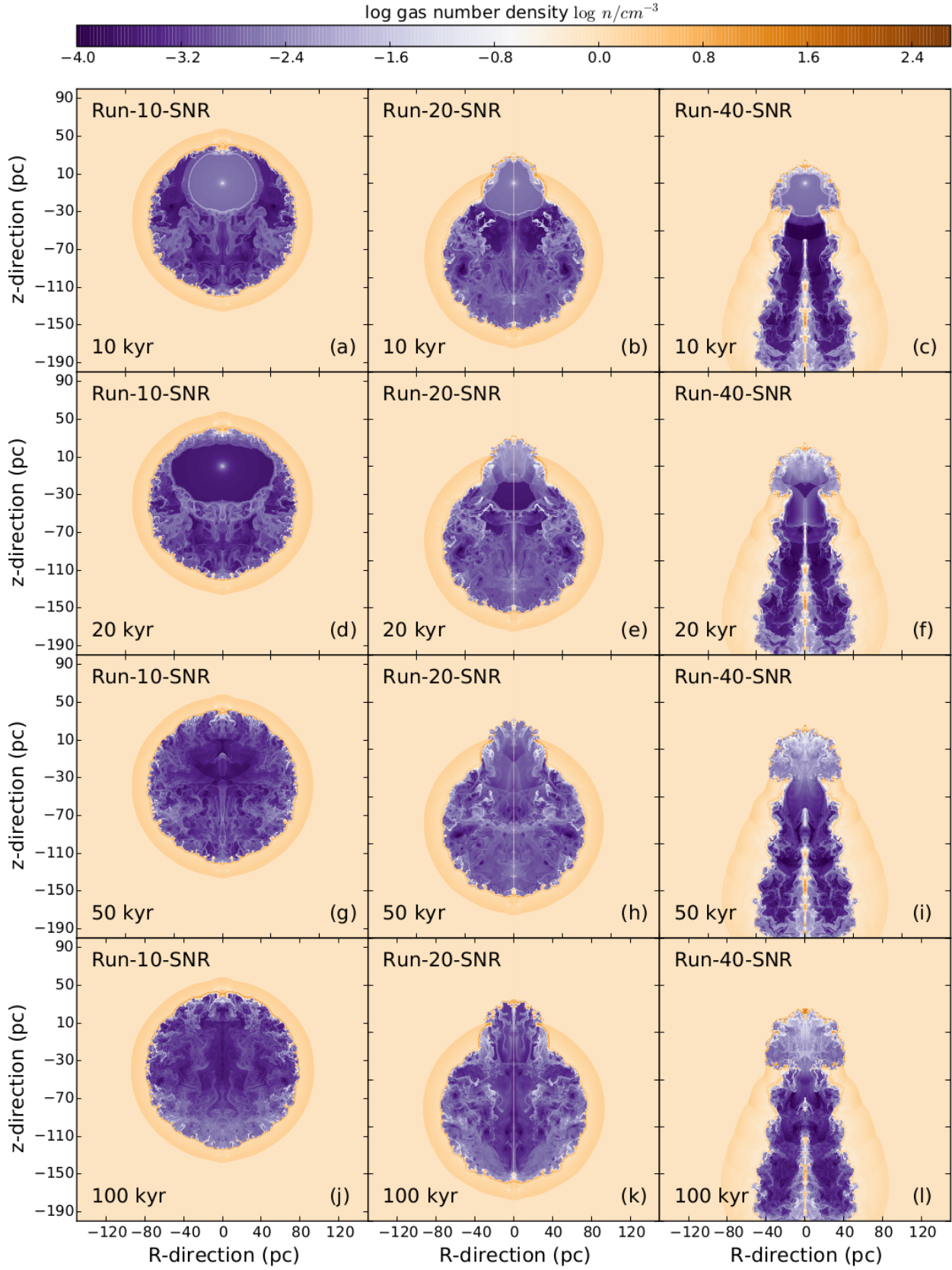


**Figure 7.** Density fields (in  $\text{cm}^{-3}$ ) of the supernova remnants generated by a moving  $60\text{-}M_{\odot}$  stars. The columns display the models Run-10-SNR (left,  $v_{\star} = 10 \text{ km s}^{-1}$ ), model Run-20-SNR (middle,  $v_{\star} = 20 \text{ km s}^{-1}$ ) and model Run-40-SNR (right,  $v_{\star} = 40 \text{ km s}^{-1}$ ). Each remnant is shown at times 10 kyr (top row, panels a-c), 20 kyr (second row, panels d-f), 50 kyr (third row, panels g-i), and 100 kyr (bottom row, panels j-l), respectively.



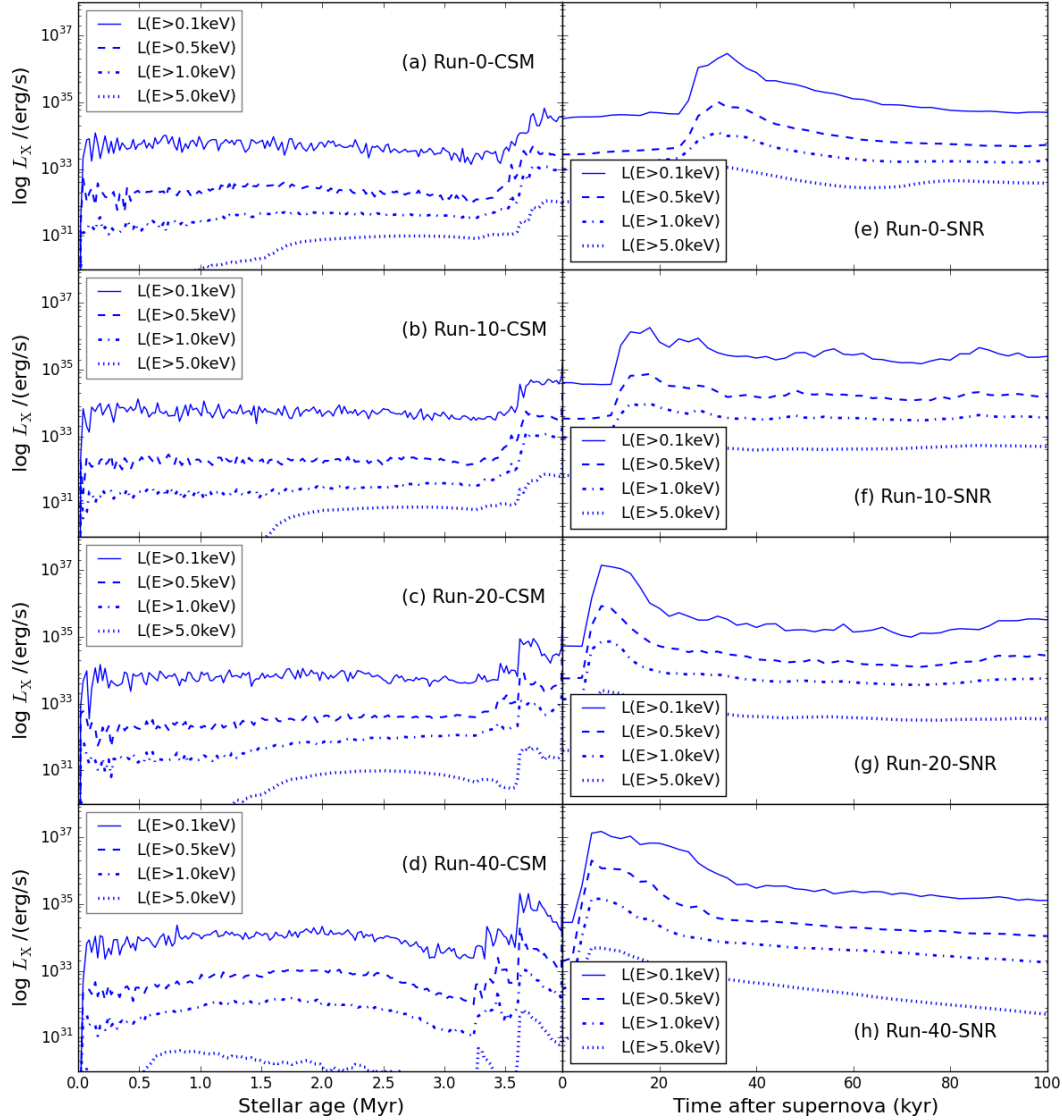


**Figure 8.** Lightcurves of thermal X-ray before (left panels) and after the supernova explosion (right panels). The integrated luminosity is plotted as a function of time, for different energy bands (in  $\text{erg s}^{-1}$ , blue lines) and for several space velocities of the progenitor, spanning from  $v_* = 0 \text{ km s}^{-1}$  (top panels) to  $v_* = 40 \text{ km s}^{-1}$  (bottom panels), respectively.

cal aspect, albeit affected by Rayleigh-Taylor instabilities (Fig. 7k). Simultaneously, the unstable shock wave expands downstream the progenitor star’s direction inside the cavity and eventually reaches the bottom of the wind bubble (Fig. 7k).

In our fast-moving model Run-40-SNR, the supernova shock first fills the Wolf-Rayet bubble, which gets heated by reverberations against the unstable post-main-sequence ring (Fig. 7c,f,i). It is then channeled as a jet-like extension to the spherical region of shocked ejecta into the tubular cavity formed by the tail of the progenitor’s bow shock with the mechanism described in Blandford et al. (1983); Cox et al. (1991). Last, the reflection of the shock wave that also happens inside the tail of the bow shock fills the main-sequence nebula with hot gas as described in Meyer et al. (2015), see Fig. 7l.

### 3.3 X-ray signature

The thermal X-ray luminosity for the circumstellar nebulae and the supernova remnants of our massive star is plotted as a function of time in Fig. 8. To predict the emission properties of our old (10 – 100 kyr) supernova remnants, we generate X-ray lightcurves (cf. Meyer et al. 2015). For each simulation snapshot, the X-ray emission coefficient,  $j_X^{E \geq \alpha}$  for the  $E \geq \alpha$  energy band, is calculated and integrated over the whole nebula,

$$L_X^{E \geq \alpha} = \iint_{\text{SNR}} j_X^{E \geq \alpha}(T) n_H^2 dV, \quad (17)$$

where  $n_H$  is the hydrogen number density in the supernova remnant (SNR). The thermal X-ray emission coefficient of the diffuse ISM is tabulated as a function of temperature with the XSPEC<sup>4</sup> soft-

<sup>4</sup> <https://heasarc.gsfc.nasa.gov/xanadu/xspec/>

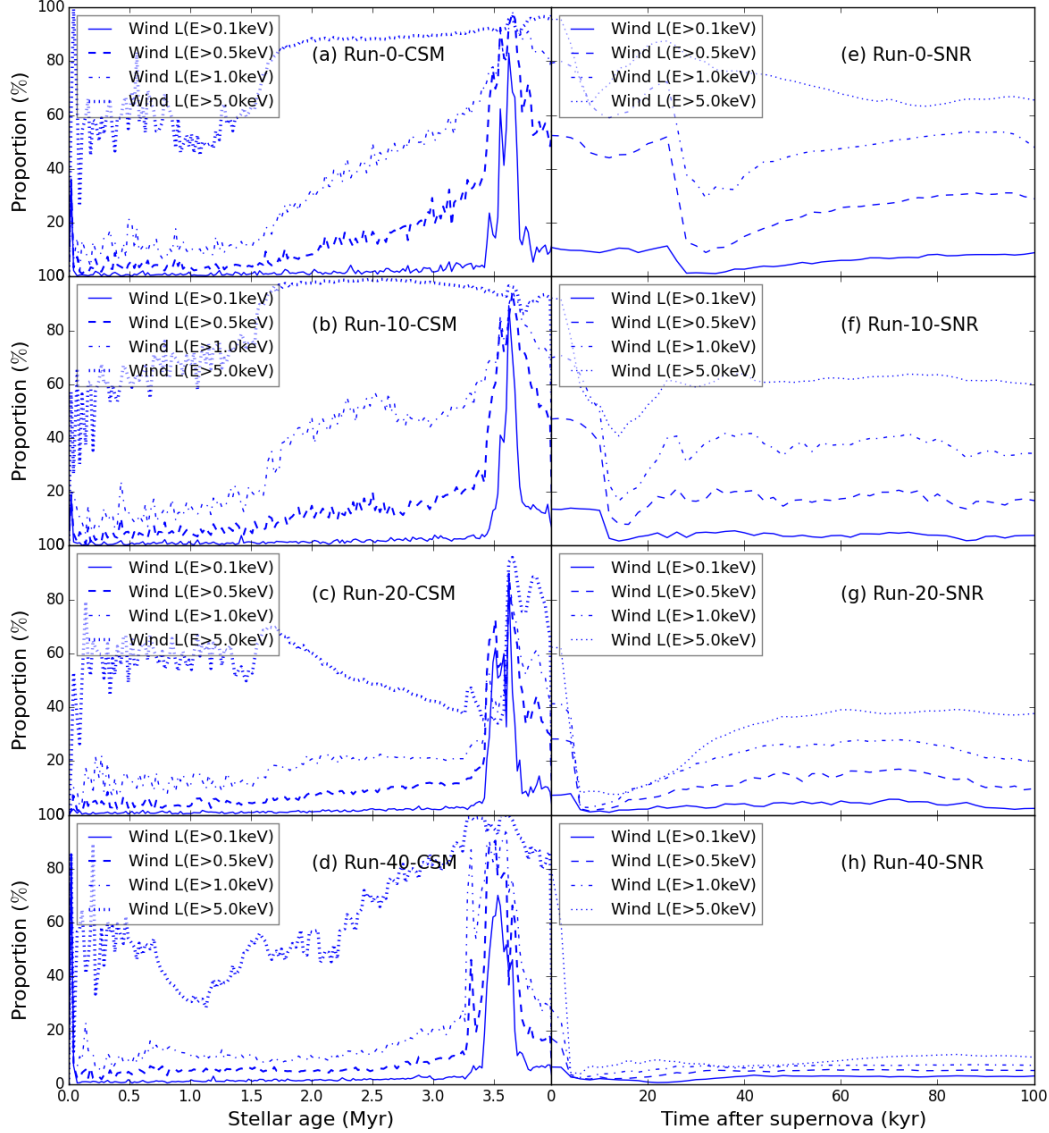


**Figure 9.** Stellar wind contributions to the thermal X-ray luminosity (in %) as a function of time for the pre-supernova epoch (left panels) and the supernova remnant phase (right panels). Each panel covers several energy bands, and each row shows results for different space velocities of the progenitor, spanning from  $v_* = 0 \text{ km s}^{-1}$  (top panels) to  $v_* = 40 \text{ km s}^{-1}$  (bottom panels), respectively.

ware (Arnaud 1996) which uses the solar abundances of Asplund et al. (2009).

The pre-supernova evolution of the thermal X-ray luminosity in our model Run-0-CSM, in which the star is at rest, begins by a rapid increase up to  $L_X^{E \geq 0.1 \text{ keV}} \approx 10^{34} \text{ erg s}^{-1}$  during the initial expansion of the wind bubble, followed by a nearly constant brightness throughout the entire main-sequence phase of the star (up to  $\approx 3.2 \text{ Myr}$ ). The small luminosity variations during this phase are caused by the instabilities in the shocked ISM. When the star moves quickly, an important mechanism is vortex shedding, described in Wareing et al. (2007) and Green et al. (2019). A slight increase of the luminosity  $L_X^{E \geq 0.1 \text{ keV}}$  coincides with the post-main-sequence evolutionary phases of the star, when the nebula reaches  $L_X^{E \geq 0.1 \text{ keV}} \approx 10^{35} \text{ erg s}^{-1}$ . This represents the fraction of the stellar wind mechanical luminosity that is not lost by, e.g., forbidden-line emission of the hot diluted gas in the shock wind region and/or by the ISM gas heated by thermal transfer (Mackey et al. 2015;

Green et al. 2019). The lightcurves in the other energy bands exhibit similar behaviour, albeit offset by 1, 2 and 4 order of magnitude for the luminosities  $L_X^{E \geq 0.5 \text{ keV}}$ ,  $L_X^{E \geq 1.0 \text{ keV}}$  and  $L_X^{E \geq 5.0 \text{ keV}}$ , respectively. The low level of  $L_X^{E \geq 5.0 \text{ keV}}$  illustrates that the hot gas ( $T \geq 10^7 \text{ K}$ ) emitting by free-free emission negligibly contributes to cooling in the nebula. The soft X-ray luminosity that we obtain from our model is consistent with predictions for nebulae around Wolf-Rayet stars, i.e. of the order of  $10^{33} \text{ erg s}^{-1}$  (Dwarkadas & Rosenberg 2013; Toalá & Guerrero 2013; Toalá et al. 2014), and the hard component from hot gas is dimmer (Chu et al. 2003). This trend is not greatly affected by the stellar motion of the high-mass star, see Fig. 8b-d, except during the post-main-sequence evolutionary phases during which the highest-energy emission,  $L_X^{E \geq 5.0 \text{ keV}}$ , exhibits stronger variations as  $v_*$  increases, reflecting the fact that the wind material released by the star interacts differently with the the main-sequence bubble an/or the ISM material, see our model Run-40-CSM at times 3.2–3.7 Myr (Fig. 8d).

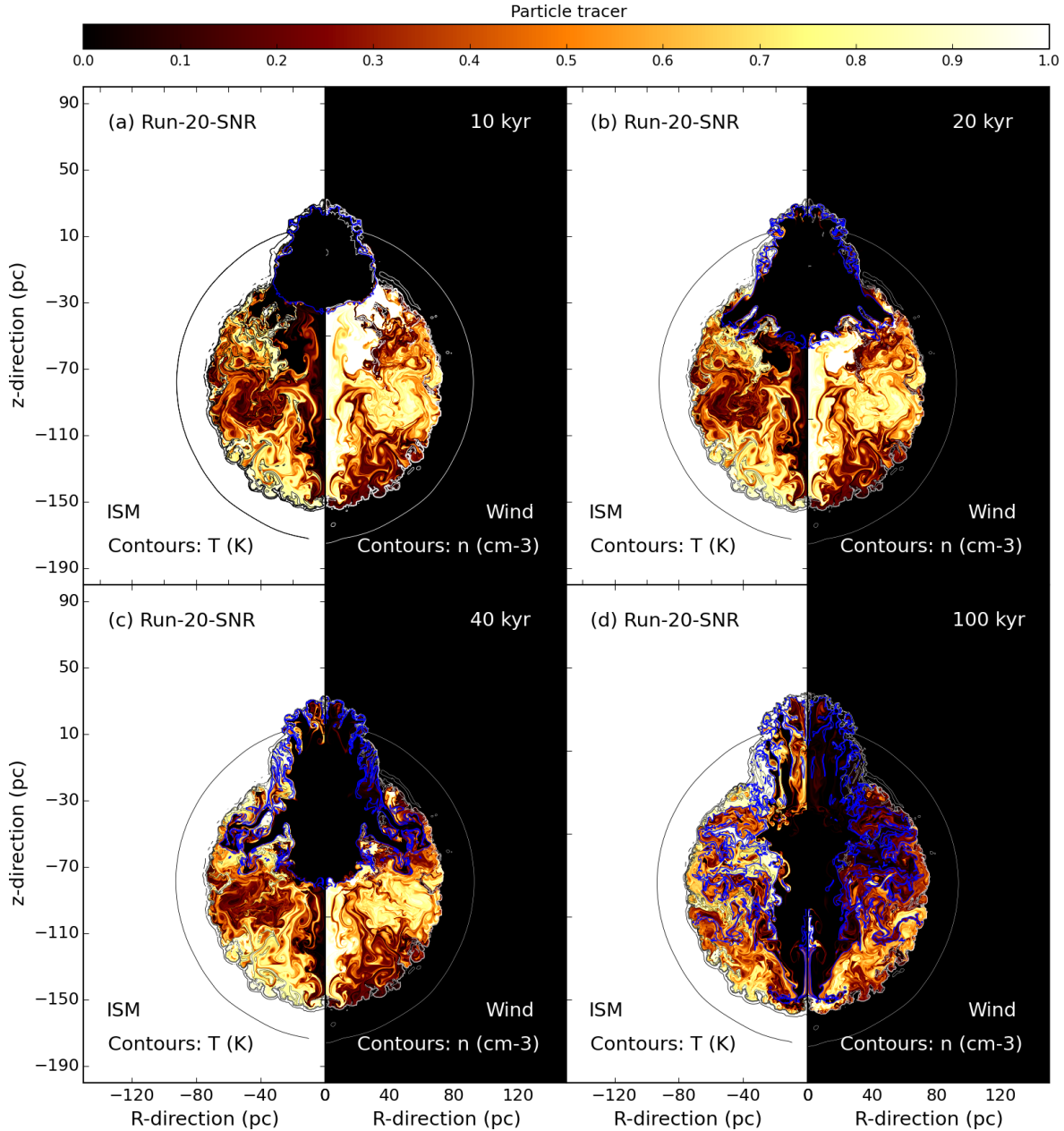


**Figure 10.** Mixing of material in the supernova remnant generated by a progenitor moving with velocity  $20 \text{ km s}^{-1}$ , shown at times 10 kyr (a), 20 kyr (b), 50 kyr (c) and 100 kyr (d). The figures plot the value of the quantity  $1-Q_1$  representing the proportion of ISM material (left part of the panels) and the value of the passive scalar tracer  $Q_1$  standing for the proportion of stellar wind gas (right part of the panels), respectively. The overplotted black contours indicate the temperature ( $T = 10^5, 10^6, 10^7 \text{ K}$ , left part of the panels) while the white contours stand for the gas number density ( $n = 1.0, 10^1, 10^2$  and  $10^3 \text{ cm}^{-3}$ , right part of the panels). The blue contours of the passive scalar field  $Q_2$  indicate a 10% contribution of ejecta in number density.

The post-supernova evolution of the thermal X-ray luminosities begins with  $L_X^{E \geq 0.1 \text{ keV}} \approx 10^{34} \text{ erg s}^{-1}$  in the static star case (Fig. 8e) and slightly more for a runaway progenitor (Fig. 8h). A sudden rise of the lightcurves happens when the forward shock collides with the wind termination shock. In the static case this happens around 25 kyr after the explosion (see Fig. 8e and Fig. 7a,d) and sooner if the bulk motion of the progenitor is larger (Fig. 8f-h) since the stand-off distance of the corresponding bow shock is smaller (Wilkin 1996). The luminosities then decrease, nonetheless, they are interspersed with additional peaks and/or variations provoked by the reflections of the reverberated shock wave onto the cavity's wall. As before the time of the explosion, the lumi-

nosities in the more energetic bands are about 1, 2 and 3 order of magnitude lower for  $L_X^{E \geq 0.5 \text{ keV}}$ ,  $L_X^{E \geq 1.0 \text{ keV}}$  and  $L_X^{E \geq 5.0 \text{ keV}}$ , respectively, i.e. the remnants of runaway progenitors are easier to observe in the soft X-ray band than in the hard X-ray band. This order relation persists throughout the expansion of the supernova remnant in the ISM (Fig. 8f-h). However, the hard X-ray emission decreases faster as function of time because the supernova remnant expands into the ISM and cools so that the hot gas contribution to the emission is less and less important (Meyer et al. 2015).

Fig. 9 plots the evolution of the stellar wind contribution to the

thermal X-ray luminosity, calculated for each energy band as,

$$L_X^{E \geq \alpha} = \iint_{\text{SNR}} j_X^{E \geq \alpha}(T) n_H^2 Q_1 dV, \quad (18)$$

where  $Q_1$  is the passive scalar discriminating stellar wind from other kinds of material. The  $E \geq 5.0\text{keV}$  luminosity mostly originates from the stellar wind while the emission at  $E \geq 1.0\text{keV}$  largely comes from the shocked ISM gas. The stellar-wind contribution to the latter is about a few per cent when the bubble grows at times  $\leq 1.5\text{Myr}$  and increases up to  $\geq 80\%$  when the star has evolved to the post-main-sequence phases, see our models Run-0-CSM and Run-10-CSM (Fig. 9a,b). In the runaway progenitor cases this contribution reaches only about 60% (Fig. 9d) which means that the expelled luminous-blue-variable and Wolf-Rayet shells emit more by thermal Bremsstrahlung than the ISM material. In the other energy bands the stellar wind contribution of their emission is negligible during the main-sequence phase, as it represents  $\leq 10\text{--}15\%$  of the overall emission, but it progressively increases when the bubble is formed at time 1.5 Myr. This changes during the Luminous-Blue-Variable and the Wolf-Rayet phases when the wind contribution to  $L_X^{E \geq 0.5\text{keV}}$  rises up to 90%. Note that for a static star  $L_X^{E \geq 0.1\text{keV}}$  exhibits variations reflecting the successive mass-loss rate variations happening during the luminous blue variable eruptions and Wolf-Rayet events (Fig. 9a). These variations of the stellar-wind contribution to  $L_X^{E \geq 0.1\text{keV}}$  are independent of the speed of the progenitor star (Fig. 9b-d).

The proportion of thermal-X-ray-emitting wind material in the supernova remnants is a function of the bulk motion of the progenitor star, and, consequently, relates on the distribution of circumstellar material at the supernova time. Its largest contribution, about 10%, arises in the  $E \geq 5.0\text{keV}$  energy band (Fig. 9e-h). This further illustrates how the contribution of stellar wind to the soft X-ray emission in the remnant decreases with gas temperature. Once the expansion of the supernova shock wave in the unperturbed stellar wind ceases ( $< 5\text{--}10\text{kyr}$ ), the wind contribution to the hard X-ray emission decreases from about 80% in the static case to below 10% for our fastest-moving progenitor. Our results highlight that thermal X-ray emission of remnants from fast-moving progenitors originates from ISM material, as most of the wind gas has been advected far from the location of the explosion and had time to cool before the moment of the blastwave-circumstellar medium interaction. Note that the figure represent the proportion of wind material exclusively, the rest originating from the sum of the shocked ISM gas plus the ejecta melting into the supernova remnant (see Section 3.4). The ejecta contribution to the thermal X-ray emission is not important compared to that of the wind and ISM because its mass is much smaller than the overall remnant mass.

### 3.4 Mixing of material

Fig. 10 illustrates the temporal evolution of the mixing of ejecta/wind/ISM material in our supernova remnant model Run-20-SNR for a progenitor star moving with speed  $v_* = 20\text{ km s}^{-1}$ . The panels correspond to the remnant at times 10 (a), 20 (b) 40 (c) and 100 kyr (d) after the explosion, respectively. On each plot, the left-hand side shows the value of  $1 - Q_1$ , i.e. the proportion of ISM gas in the computational domain and the right-hand side shows the value of the tracer  $Q_1$  for the stellar wind material, respectively, both spanning from 0 to 1, with 0 standing for the complete absence of a given species while 1 stands for a medium exclusively made of this kind of species, respectively. The black contours indicate the locations where the remnant temperature is  $T = 10^5$ ,

$10^6$ , and  $10^7\text{ K}$ , while the white lines are iso-contours for the gas density with levels  $n = 1.0, 10^1, 10^2$ , and  $10^3\text{ cm}^{-3}$ . Additionally, the overplotted blue contours trace the regions at which ejecta contributes 10% of the gas.

After 10 kyr the supernova blastwave bounces against the ring opened by the final Wolf-Rayet wind of the defunct star, where it is partially reverberated towards the center of the explosion and partially transmitted to the ISM through the bow shock according to the mechanism described in Borkowski et al. (1992); Meyer et al. (2015). The supernova remnant is mostly filled with hot stellar-wind gas surrounded by a main-sequence shell of dense, cold ISM material. The interface between wind and ISM is the former unstable contact discontinuity of the pre-supernova bubble with which the various post-main-sequence shells collided (Fig. 10a). After 20 to 40 kyr the supernova shock wave that passed through the Wolf-Rayet wind keeps on expanding into the unperturbed ISM, and the reflection of its forward shock to the center of the explosion begins, enhancing the mixing of stellar wind and ISM material. This is the process which is responsible for the formation of Cygnus-loop supernova remnant, although that particular objects concerns a lower-mass, red supergiant progenitor (Meyer et al. 2015; Fang et al. 2017).

Simultaneously, the reverberated shock wave develops instabilities at the interface between ejecta and mixed wind/ISM material (Fig. 10b,c) while the region occupied by the ejecta further expands into the interior of the wind blown cavity (Fig. 10c). After 40 kyr the supernova remnant assumes an asymmetric morphology made of the large, spherical, former main-sequence bubble (lower part) and the Wolf-Rayet-produced cocoon (upper part). The bubble concentrates the stellar wind material surrounded by a layer of shocked ISM mixed with ejecta material while the almost ejecta-free upper mushroom is filled with a mixture of wind and ISM gas. The ejecta material lies in a tubular zone located at the inside of the bottom region of the remnant, directed towards to the direction of motion of the supernova progenitor, as well as in the region to the former center of the explosion (Fig. 10d).

Fig. 11 is similar to Fig. 10 for our model Run-40-SNR with a runaway progenitor star moving at  $v_* = 40\text{ km s}^{-1}$ . As the progenitor rapidly moves, the main-sequence bubble is elongated. The blastwave bounces against the stellar wind bow shock of the progenitor which is separated from the nebula that was produced during its main-sequence phase of evolution. This advects the ejecta all across the Wolf-Rayet shell-like region generated during the progenitor's ultimate evolutionary stage, which is centered onto the location of the explosion (Fig. 11a,b). Between 20 kyr and 40 kyr the shock-wave/Wolf-Rayet-shell interaction continues, and so does the mixing of material, as part of the supernova shock wave expands into the low-density cavity of unperturbed wind material, along the direction opposite of the motion of the progenitor. Pushed downward by the ejecta, the former unperturbed shocked stellar wind develops instabilities at its interface with the shocked ISM (Fig. 11b,c).

At time 40 kyr the supernova remnant has an internal structure different from that of Run-20-SNR (with  $v_* = 20\text{ km s}^{-1}$ ). It is made of an upper quasi-circular region and a longer, tail-like structure. Both regions have efficiently mixed stellar wind and ISM gas. The ejecta are both located in the upper cocoon and in the main-sequence wind bubble (Fig. 11d). Models Run-20-SNR and Run-40-SNR reveal the importance of progenitor motion in the mixing of different materials in remnants of massive runaway progenitors. The degree of wind/ISM mixing and the distances from the center of the explosion at which it happens increases with  $v_*$

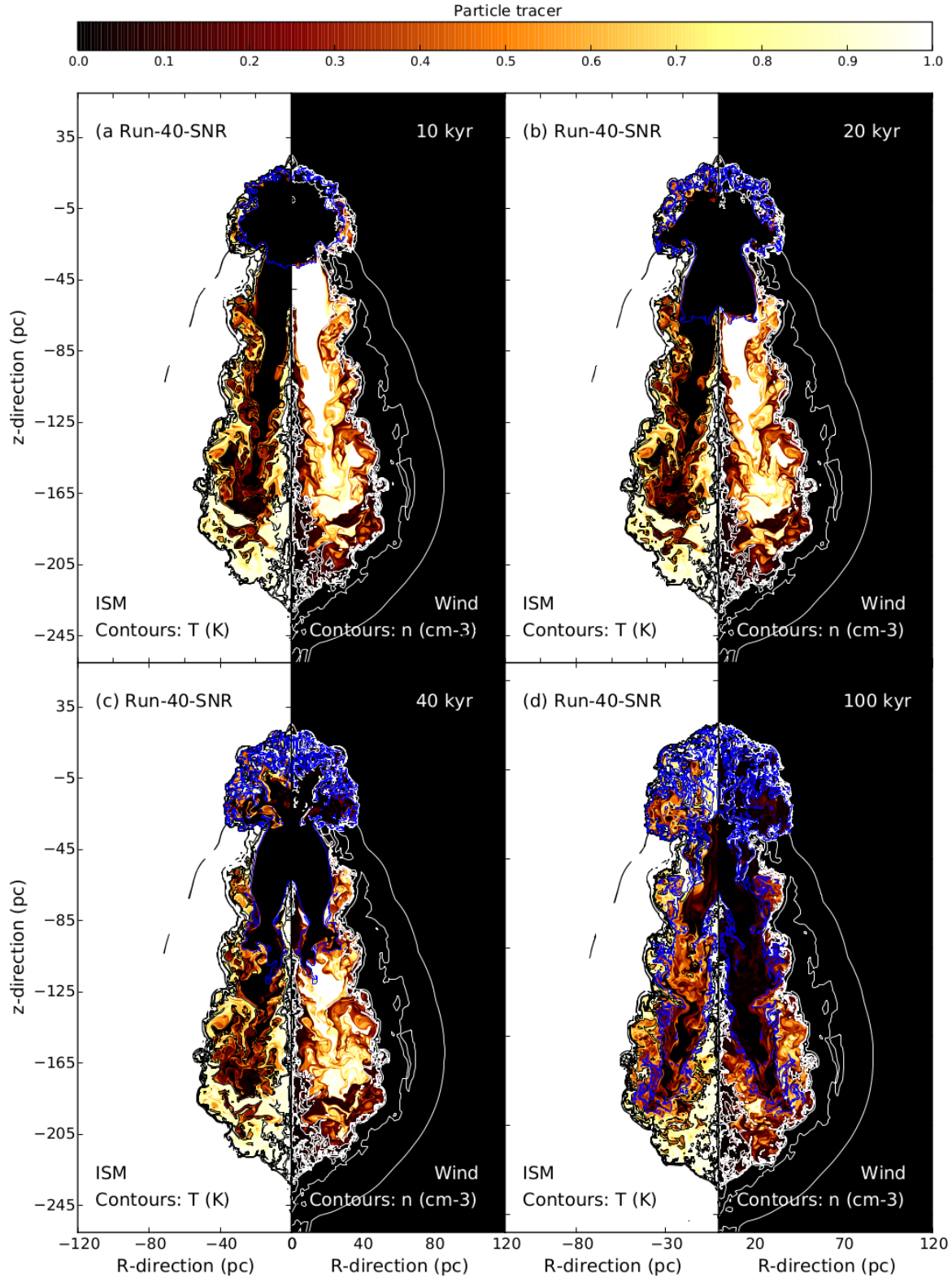


**Figure 11.** Same as Fig. 10 but here for a progenitor moving with velocity  $40 \text{ km s}^{-1}$ . The figures plot the value of the quantity  $1-Q_1$  representing the proportion of ISM material (left part of the panels) and the value of the passive scalar tracer  $Q_1$  standing for the proportion of stellar wind gas (right part of the panels), respectively. The blue contours of the passive scalar field  $Q_2$  indicate a 10% contribution of ejecta in number density.

(Fig. 10d, Fig. 11d) as a consequence of the elongation of the stellar wind bubble. It channels the supernova shock wave when the Mach number of the progenitor moving through the ambient medium is  $v_*/c_s \sim 2$ , with  $c_s$  the unperturbed ISM sound speed, while the ejecta distribution remains is spherical only if the progenitor is either at rest or slowly-moving and explode inside and/or off-centered in its main-sequence circumstellar bubble, at least in the ambient medium that we consider.

## 4 DISCUSSION

This section presents the limitations of our method, discusses our results in the context of previous studies, compares our results with observations of asymmetric supernova remnants, and further discusses the potential role of stellar wind nebula as cosmic-ray accelerators.

### 4.1 Caveats of the models

The first limitation of our method is the two-dimensional nature of the hydrodynamical simulations, which restricts the realism of the modelled wind bubbles and supernova remnants. Axisymmetry in particular prevents us from investigating the effects of, e.g., the angles between the direction of motion of the progenitor star, the local interstellar magnetic field, and the axis of stellar rotation. Three-dimensional simulations such as in Katushkina et al. (2017, 2018) would be highly desirable for a more realistic depiction of the surroundings of massive stars, however, their huge computational costs would inhibit scanning the parameter space. The treatment of the intrinsic nature of the ISM is simplified by assuming a uniform medium of number density  $1 \text{ cm}^{-3}$  and temperature 8000 K (Meyer et al. 2014). Any intrinsic native turbulence in the velocity field of the medium, clumps, or filamentary structures that could potentially influence the development of shocks wave are also neglected, see Gvaramadze et al. (2018). The stellar wind history used as boundary conditions is also not unique, and other evolutionary tracks and alternative stellar rotation rates can change the luminous blue variable or the Wolf-Rayet phase of massive stars (Ekström et al. 2012). They would produce a different wind bubble and consequently result in dissimilar supernova remnants.

### 4.2 Comparison with previous studies

Our method uses a self-consistently calculated stellar evolution history as boundary for the stellar wind, and the hydrodynamical simulations are performed for a different corner of the parameter space and on a higher spatial grid resolution than in other studies. Previous works tackled the problem of the circumstellar medium of Wolf-Rayet-evolving stars either considering static stars (Garcia-Segura & Mac Low 1995; Garcia-Segura et al. 1996) or using lower-resolution calculations of moving stars in the context of the formation of dense circumstellar regions eventually leading to gamma-ray bursts (Eldridge et al. 2006; van Marle et al. 2006, 2007; Eldridge et al. 2011). The series of work of Brighenti & D’Ercole (1994, 1995b,a) is the closest to our approach in the sense that it explores the morphology of wind bubbles blown by massive stars by first calculating the evolution of their surroundings before launching a blastwave in it.

Only one study of this series investigates the shape of supernova remnants from moving Wolf-Rayet progenitors, although not primarily undergoing luminous-blue-variable eruptions (Brighenti &

D’Ercole 1994). Their model 1 has ISM properties and a stellar motion similar to our run Run-20-SNR, however, assuming a different stellar wind history as it includes a cool red supergiant phase while we here simulate luminous blue variable and Wolf-Rayet stars. A slowly-moving progenitor (our calculations Run-10-CSM and Run-10-SNR) is also not considered in that work. Last, a couple of works have been tailored to the study of specific young supernova remnants, whose shape might be explained by the presence of a bow shock around the progenitor prior to its explosion. These studies mainly concern the Crab nebula (Cox et al. 1991) and the Kepler supernova remnant (Borkowski et al. 1992; Velázquez et al. 2006; Chiotellis et al. 2012; Toledo-Roy et al. 2014). These models apply to much younger ( $\sim 1000 \text{ yr}$ ) supernova remnants than ours and cover a different corner of the problem’s parameter space.

### 4.3 Comparison with observations

#### 4.3.1 Comparison with existing wind nebulae: the case of BD+43°3654

The most obvious object permitting a comparison with our models for the pre-supernova circumstellar medium of the  $60 M_\odot$  of Groh et al. (2014) is the very massive  $\simeq 55\text{--}85 M_\odot$  runaway star BD+43°3654, which probably escaped from the Cygnus OB2 region (Comerón & Pasquali 2007). BD+43°3654 is an  $\approx 1.6 \text{ Myr}$ -old, O4If-typed main-sequence stellar object stellar which properties have been constrained to be  $\dot{M} \approx 10^{-5} M_\odot \text{ yr}^{-1}$  and  $v_w \approx 2300 \text{ km s}^{-1}$ , respectively. Its surrounding is shaped as a well-defined, axisymmetric bow-shock nebula visible in the infrared. Using the observed geometry of the bow shock, its proper motion has been estimated to be  $\approx 40 \text{ km s}^{-1}$  and its ambient medium density to be  $n_{\text{ISM}} = 6 \text{ cm}^{-3}$  (Comerón & Pasquali 2007).

Nevertheless, the formula for the stand-off distance of a bow shock measured along the direction of motion of its driving star,

$$R_{\text{SO}} = \sqrt{\frac{\dot{M} v_w}{4n_{\text{ISM}} v_*^2}}, \quad (19)$$

informs that  $n_{\text{ISM}}$  is a function of  $\dot{M}$  (Baranov et al. 1971; Wilkin 1996) and the discoverers of BD+43°3654’s bow shock discussed in Comerón & Pasquali (2007) that any overestimate of the wind properties  $\dot{M}$  or  $v_w$  will translate into a overestimate of its background ISM density, which may therefore be smaller than  $n_{\text{ISM}} = 6 \text{ cm}^{-3}$  by a factor of  $\approx 3$ . This is comparable with the value of  $\simeq 0.79 \text{ cm}^{-3}$  used in our study. By interpolating our stellar evolutionary track, we find  $\dot{M} \approx 10^{-5} M_\odot \text{ yr}^{-1}$  and  $v_w \approx 2865 \text{ km s}^{-1}$  for the stellar age of BD+43°3654  $\approx 1.6 \text{ Myr}$ , that is rather consistent with the derivations of Comerón & Pasquali (2007). Hence, our model Run-40-CSM fits well the case of BD+43°3654 and our simulation can be considered as a prediction of the future evolution of its pre- and eventual post-supernova circumstellar medium.

#### 4.3.2 Comparison with existing supernova remnants

We note that Brighenti & D’Ercole (1994, 1995a) proposed that barrel-shaped supernova remnants such as G296.5+10.0 (Storey et al. 1992; Harvey-Smith et al. 2010) and other bipolar remnants of similar morphology (Bisnovatyi-Kogan et al. 1990) have been generated by the interaction between a supernova shock wave with the walls of a low-density wind cavity produced by the stellar motion of its own progenitor, into which the forward shock has been channeled (Cox et al. 1991). This idea has been supported by Meyer

et al. (2015) with optical H $\alpha$  and [OIII] synthetic emission maps derived from hydrodynamical simulations of red-supergiant-evolving runaway progenitor stars. However, most such supernova remnants have been shown to be aligned with the galactic magnetic field and directed towards the Galactic center. This observational evidence suggests that their formation is better explained as effect of the interstellar magnetic field in Galactic spiral arms (Gaensler 1998). This hypothesis has been supported with both magneto-hydrodynamical simulations and non-thermal synchrotron and radio emission maps (Orlando et al. 2007).

We can also see noticeable differences between our supernova remnants models generated by runaway luminous blue variable/Wolf-Rayet progenitors and those for runaway red supergiant progenitors (see Meyer et al. 2015). In the case of a red supergiant progenitor, the ejecta blows out beyond the last wind bow shock and freely expands into the ISM, if the progenitor moves sufficiently fast and/or if the stellar wind is not too dense. A heavier ZAMS stars and/or a slower progenitor generate a denser bow shock of swept-up ISM which will trap the new-born cold red supergiant shell and the subsequent shock wave. This feature is present in all of our runaway ( $v_* \geq 20 \text{ km s}^{-1}$ ) Wolf-Rayet progenitor runs. One should therefore expect to observe remnant from runaway Wolf-Rayet progenitor with Cygnus-Loop-nebula-like morphology, which would resemble a remnant of a runaway red supergiant-evolving star (Tenorio-Tagle et al. 1985; Aschenbach & Leahy 1999; Meyer et al. 2015; Fang et al. 2017), although of different size and chemical composition. Inversely, our results argue against a  $60 M_{\odot}$  ZAMS star as progenitor of historical supernova remnants such as Kepler's or Tycho and support solutions involving symbiotic binary systems of a runaway AGB star together with an type Ia explosive companion (Borkowski et al. 1992; Velázquez et al. 2006; Vigh et al. 2011; Chiotellis et al. 2012; Williams et al. 2013; Toledo-Roy et al. 2014).

The supernova remnant G109.1-1.0 (CTB 109) has for long been suspected to be an isolated supernova remnant whose progenitor may have moved quickly (Brighenti & D'Ercole 1994, 1995a). However, evidence of dense molecular material aside of the remnant (Sánchez-Cruces et al. 2018) suggests it being produced by a shock wave evolving into a rather low-density medium that is sparsely with higher-density cloudlets (Coe et al. 1989; Sasaki et al. 2006), see also the numerical simulations of Bolte et al. (2015). The remnant VRO 42.05.01 (Arias et al. 2019) may be the archetypal example of a supernova remnant interacting with an ISM cavity. The low-density region inducing the asymmetries may have been formed by a previous supernova (Rho & Petre 1997) or by the motion of the progenitor star itself (Derlopa et al. 2019). Recent observations of molecular emission and numerical studies tailored to VRO 42.05.01 suggest that the progenitor could have been a massive runaway star interacting with a hot diluted ISM tunnel (Derlopa et al. 2019), but indicated also that an asymmetric Wolf-Rayet wind is sufficient to produce its overall morphology (Chiotellis et al. 2019). The influence of the anisotropy of post-main-sequence stellar winds should be investigated in future studies. The supernova remnant S147 has been suggested to result from a Wolf-Rayet progenitor (Gvaramadze 2006) in a multiple system (Dinçel et al. 2015).

#### 4.4 Are Wolf-Rayet nebulae efficient cosmic rays accelerators ?

There is a growing interest in the non-thermal surroundings of massive stars. The strong winds of OB and Wolf-Rayet stars gener-

ate magnetised termination shocks such that a proportion of the stellar mechanical luminosity could power high-energy cosmic rays (Webb et al. 1985; Seo et al. 2018). A number of numerical simulations calculating the acceleration and diffusion of cosmic rays in static stellar-wind/bow-shock environments of massive stars have been performed (del Valle et al. 2013, 2015; del Valle & Pohl 2018), and speculative predictions were announced for the Bubble nebula, a runaway OB star moving through dense molecular gas (Green et al. 2019). Particle acceleration and the production of non-thermal emission in the surroundings of pre-supernova (runaway) massive stars are expected to arise from processes similar to those operating in young supernova remnants (Reynolds 2011), albeit with smaller efficiency (Voelk & Forman 1982; Zirakashvili & Ptuskin 2018).

Per object, circumstellar cosmic-ray feedback of high-mass stars is of lower importance in the Galactic energy budget compare to other non-thermal-emitting objects such as supernova remnants (Seo et al. 2018; Rangelov et al. 2019) or colliding winds in binaries (Benaglia & Romero 2003; De Becker et al. 2006; Reimer et al. 2006; De Becker & Rauq 2013). Accordingly non-thermal X-rays from stellar-wind bow shocks surrounding OB stars have not been detected to date (Toalá et al. 2016; De Becker et al. 2017; Toalá et al. 2017; Binder et al. 2019). Prajapati et al. (2019) recently claimed the detection of synchrotron emission from a series of shells and arc around the Wolf-Rayet nebula G2.4+1.4. Our results further explore the circumstellar medium of evolved massive stars and provide the background on which we shall investigate the synchrotron, inverse Compton and Gamma-ray emission, e.g. using the RATPAC code (Telezhinsky et al. 2012b,a, 2013).

## 5 CONCLUSION

Motivated by the existence of stars, whose mass exceeds  $\sim 60 M_{\odot}$  and which can either be affected by high proper motion and/or generate circumstellar nebulae by stellar wind-ISM interaction (Tatischeff et al. 2010; Gvaramadze & Gualandris 2011; Gvaramadze et al. 2013), we investigate the shaping of circumstellar nebulae around a non-rotating  $60 M_{\odot}$  stars (Groh et al. 2014) and we explore how they can influence the development of asymmetries in their supernova remnants. These stars are characterised by a violent evolution history including several successive luminous-blue-variable and Wolf-Rayet phases. Using high-resolution 2D hydrodynamical simulations performed with the PLUTO code (Mignone et al. 2007, 2012), we investigate how the ejection of the dense shells associated to these evolutionary phases can couple to the stellar proper motion and carve aspherical low-density cavities of wind material, inside of which the star dies as a core-collapse supernova. The resulting remnant therefore adopts anisotropies reflecting the imprint of star's past evolution history onto its close surroundings (Meyer et al. 2015). We consider several static, slowly-moving, and fast stars evolving in the warm phase of the ISM, and we predict the thermal X-ray signature of both their stellar wind nebulae and supernova remnants up to 100 kyr after the explosion.

We show that, as long as such a massive ( $\sim 60 M_{\odot}$ ) progenitor star moves supersonically through the ISM, its subsequent supernova remnant will display similarity to that of the Cygnus-loop nebulae. The role of the strong luminous-blue-variable and Wolf-Rayet shells winds predicted by the Geneva stellar evolutionary tracks (Groh et al. 2014) add to the asymmetries produced by the stellar motion as they induce outflows that can pierce the main-sequence wind bubble of the progenitor star, opening a route

for the later supernova shock wave. A rather modest bulk motion ( $10 \text{ km s}^{-1}$ ) of our  $60 M_{\odot}$  star is not sufficient to break the sphericity of the overall remnant as the expanding supernova shock wave is trapped into the defunct, quasi-spherical stellar wind bubble (Weaver et al. 1977).

However, as the progenitor star moves faster, the explosion is off-set with respect to the geometrical center of the wind nebula and, in the runaway limit of the stellar motion, happens outside of the bubble, in a ring of Wolf-Rayet and ISM material. The shock wave blows out of the wind nebula, resulting in an homogeneous mixing of material throughout the elongated remnant, while ejecta is reverberated around the center of the explosion. This leads to the formation of two-lobes structures ahead and behind the center of the explosion, inside of which the degree of mixing of ejecta with wind and ISM materials is correlated to the progenitor's motion. Our pre-supernova nebulae and supernova remnants are bright in soft thermal X-rays from shocked ISM gas, except during the luminous-blue-variable eruptions of the progenitor when it comes from the stellar wind. Additionally, such remnants of low-velocity progenitors exhibit a hard X-rays component of shocked stellar wind.

Our results stress that a single runaway high-mass star can affect the chemical composition of an entire local region of the ISM, see e.g. Tatischeff et al. (2010). Consequently, we highlight the importance of chemically investigating the large-scale surroundings ( $\sim 100 \text{ pc}$ ) of supernova remnants, as it is a trace of the possible runaway nature of the defunct star(s), but also since the distribution of enriched material that has mixed in it with the ISM informs on the past stellar evolution of supernova progenitor(s). Furthermore, our simulated remnants indicate that luminous-blue-variable/Wolf-Rayet-type progenitors can not be the origin of supernova remnants with morphologies such as those of Cas A, RCW86, Kepler or Tycho. Their young age ( $\leq 2500 \text{ yr}$ ) and compact size are not in accordance with our results, which either support scenarios involving type Ia supernova and/or suggest a non-Wolf-Rayet-evolving core-collapse progenitor. Stellar wind-ISM interaction should therefore be further investigated by scanning the parameter study of the problem and by modelling such remnants with, e.g. global 3D magneto-hydrodynamical simulations. Particularly, the large termination shocks which form around luminous-blue-variable and Wolf-Rayet stars suggest that these wind nebulae might accelerate particles as high-energy cosmic rays. This is consistent with the recent monitoring of synchrotron emission from the Wolf-Rayet shell nebula G2.4+1.4 (Prajapati et al. 2019) and motivates future observational and theoretical studies on the non-thermal emission of circumstellar structures such as synchrotron and inverse Compton radiation.

## ACKNOWLEDGEMENTS

The authors thank the anonymous referee for comments which improved the quality of the paper. DMAM and M. Pohl acknowledge B. Hnatyk for constructive discussion. The authors acknowledge the North-German Supercomputing Alliance (HLRN) for providing HPC resources that have contributed to the research results reported in this paper. M. Petrov acknowledges the Max Planck Computing and Data Facility (MPCDF) for providing data storage resources and HPC resources which contributed to test and optimise the PLUTO code. This research made use of the PLUTO code developed at the University of Torino by A. Mignone and collaborators, the Matplotlib plotting library for the Python programming lan-

guage and the XSPEC X-ray spectral fitting package developed by K. Arnaud and collaborators at the University of Maryland. DMAM thanks the Lorentz Center at the University of Leiden for organising and hosting the workshop "Historical Supernovae, Novae and Other Transient Events" in October 2019, where many insightful discussions which participated to the completion of this paper took place.

## REFERENCES

- Arias M., Vink J., Iacobelli M., Domček V., Haverkorn M., Oonk J. B. R., Polderman I., Reich W., White G. J., Zhou P., 2019, *A&A*, 622, A6
- Arnaud K. A., 1996, in Jacoby G. H., Barnes J., eds, *Astronomical Data Analysis Software and Systems V* Vol. 101 of *Astronomical Society of the Pacific Conference Series*, XSPEC: The First Ten Years. p. 17
- Aschenbach B., Leahy D. A., 1999, *A&A*, 341, 602
- Asplund M., Grevesse N., Sauval A. J., Scott P., 2009, *ARA&A*, 47, 481
- Baranov V. B., Krasnobaev K. V., Kulikovskii A. G., 1971, *Soviet Physics Doklady*, 15, 791
- Benaglia P., Romero G. E., 2003, *A&A*, 399, 1121
- Binder B. A., Behr P., Povich M. S., 2019, *AJ*, 157, 176
- Bisnovatyi-Kogan G. S., Lozinskaia T. A., Silich S. A., 1990, *Ap&SS*, 166, 277
- Blaauw A., 1993, in Cassinelli J. P., Churchwell E. B., eds, *Massive Stars: Their Lives in the Interstellar Medium* Vol. 35 of *Astronomical Society of the Pacific Conference Series*, *Massive Runaway Stars*. p. 207
- Blandford R. D., Kennel C. F., McKee C. F., Ostriker J. P., 1983, *Nature*, 301, 586
- Blondin J. M., Koerwer J. F., 1998, *New Ast.*, 3, 571
- Bolte J., Sasaki M., Breitschwerdt D., 2015, *A&A*, 582, A47
- Borkowski K. J., Blondin J. M., Sarazin C. L., 1992, *ApJ*, 400, 222
- Brighenti F., D'Ercole A., 1994, *MNRAS*, 270, 65
- Brighenti F., D'Ercole A., 1995a, *MNRAS*, 277, 53
- Brighenti F., D'Ercole A., 1995b, *MNRAS*, 273, 443
- Chevalier R. A., 1982, *ApJ*, 258, 790
- Chiotellis A., Boumis P., Derlopa S., Steffen W., 2019, *arXiv e-prints*, p. arXiv:1909.08947
- Chiotellis A., Schure K. M., Vink J., 2012, *A&A*, 537, A139
- Chu Y.-H., Guerrero M. A., Gruendl R. A., García-Segura G., Wendker H. J., 2003, *ApJ*, 599, 1189
- Coe M. J., Davies S. R., Fahlman G. G., Gregory P. C., 1989, *MNRAS*, 238, 649
- Comerón F., Kaper L., 1998, *A&A*, 338, 273
- Comerón F., Pasquali A., 2007, *A&A*, 467, L23
- Cox C. I., Gull S. F., Green D. A., 1991, *MNRAS*, 250, 750
- Cox N. L. J., Kerschbaum F., van Marle A.-J., Decin L., Ladjal D., Mayer A., 2012, *A&A*, 537, A35
- De Becker M., del Valle M. V., Romero G. E., Peri C. S., Benaglia P., 2017, *MNRAS*, 471, 4452
- De Becker M., Raucq F., 2013, *A&A*, 558, A28
- De Becker M., Rauw G., Sana H., Pollock A. M. T., Pittard J. M., Blomme R., Stevens I. R., van Loo S., 2006, *MNRAS*, 371, 1280
- del Valle M. V., Pohl M., 2018, *ApJ*, 864, 19
- del Valle M. V., Romero G. E., 2014, *A&A*, 563, A96
- del Valle M. V., Romero G. E., De Becker M., 2013, *A&A*, 550, A112
- del Valle M. V., Romero G. E., Santos-Lima R., 2015, *MNRAS*, 448, 207
- Derlopa S., Boumis P., Chiotellis A., Steffen W., Akras S., 2019, *arXiv e-prints*, p. arXiv:1909.06131
- Dgani R., van Buren D., Noriega-Crespo A., 1996, *ApJ*, 461, 372
- Diñel B., Neuhäuser R., Yerli S. K., Anay A., Tetzlaff N., Torres G., Mugrauer M., 2015, *MNRAS*, 448, 3196
- Dwarkadas V. V., 2007, *ApJ*, 667, 226
- Dwarkadas V. V., Rosenberg D. L., 2013, *High Energy Density Physics*, 9, 226
- Dyson J. E., 1975, *Ap&SS*, 35, 299
- Dyson J. E., Gulliford P., 1975, *Ap&SS*, 37, 477



- Ekström S., Georgy C., Eggenberger P., Meynet G., Mowlavi N., Wyttenbach A., Granada A., Decressin T., Hirschi R., Frischknecht U., Charbonnel C., Maeder A., 2012, *A&A*, 537, A146
- Eldridge J. J., Genet F., Daigne F., Mochkovitch R., 2006, *MNRAS*, 367, 186
- Eldridge J. J., Langer N., Tout C. A., 2011, *MNRAS*, 414, 3501
- Fang J., Yu H., Zhang L., 2017, *MNRAS*, 464, 940
- Franco J., Tenorio-Tagle G., Bodenheimer P., Rozyczka M., 1991, *PASP*, 103, 803
- Freyer T., Hensler G., Yorke H. W., 2003, *ApJ*, 594, 888
- Freyer T., Hensler G., Yorke H. W., 2006, *ApJ*, 638, 262
- Gaensler B. M., 1998, *ApJ*, 493, 781
- Garcia-Segura G., Langer N., Mac Low M.-M., 1996, *A&A*, 316, 133
- Garcia-Segura G., Mac Low M.-M., 1995, *ApJ*, 455, 145
- Garcia-Segura G., Mac Low M.-M., Langer N., 1996, *A&A*, 305, 229
- Gies D. R., 1987, *ApJS*, 64, 545
- González R. F., Koenigsberger G., 2014, *A&A*, 561, A105
- Gräfener G., Owocki S. P., Grassitelli L., Langer N., 2017, *A&A*, 608, A34
- Grassitelli L., Langer N., Grin N. J., Mackey J., Bestenlehner J. M., Gräfener G., 2018, *A&A*, 614, A86
- Green S., Mackey J., Haworth T. J., Gvaramadze V. V., Duffy P., 2019, *A&A*, 625, A4
- Groh J. H., Meynet G., Ekström S., Georgy C., 2014, *A&A*, 564, A30
- Gull T. R., Sofia S., 1979, *ApJ*, 230, 782
- Gvaramadze V. V., 2006, *A&A*, 454, 239
- Gvaramadze V. V., Alexashov D. B., Katushkina O. A., Kniazev A. Y., 2018, *MNRAS*, 474, 4421
- Gvaramadze V. V., Gualandris A., 2011, *MNRAS*, 410, 304
- Gvaramadze V. V., Kniazev A. Y., Chene A. N., Schnurr O., 2013, *MNRAS*, 430, L20
- Gvaramadze V. V., Menten K. M., Kniazev A. Y., Langer N., Mackey J., Kraus A., Meyer D. M.-A., Kamiński T., 2014, *MNRAS*, 437, 843
- Hainich R., Rühling U., Todt H., Oskinova L. M., Liermann A., Gräfener G., Foellmi C., Schnurr O., Hamann W. R., 2014, *A&A*, 565, A27
- Harvey-Smith L., Gaensler B. M., Kothes R., Townsend R., Heald G. H., Ng C. Y., Green A. J., 2010, *ApJ*, 712, 1157
- Henney W. J., Arthur S. J., 2019a, *MNRAS*, 486, 3423
- Henney W. J., Arthur S. J., 2019b, *MNRAS*, 486, 4423
- Henney W. J., Arthur S. J., 2019c, *arXiv e-prints*, p. arXiv:1904.00343
- Henney W. J., Arthur S. J., de Colle F., Mellema G., 2009, *MNRAS*, 398, 157
- Hummer D. G., 1994, *MNRAS*, 268, 109
- Humphreys R. M., Davidson K., Hahn D., Martin J. C., Weis K., 2017, *ApJ*, 844, 40
- Huthoff F., Kaper L., 2002, *A&A*, 383, 999
- Jorissen A., Mayer A., van Eck S., Ottensamer R., Kerschbaum F., Ueta T., Bergman P., Blommaert J. A. D. L., Decin L., Groenewegen M. A. T., Hron J., Nowotny W., Olofsson H., Posch T., Sjouwerman L. O., Vandebussche B., Waelkens C., 2011, *A&A*, 532, A135
- Kaper L., van Loon J. T., Augusteijn T., Goudfrooij P., Patat F., Waters L. B. F. M., Zijlstra A. A., 1997, *ApJ*, 475, L37
- Katushkina O. A., Alexashov D. B., Gvaramadze V. V., Izmodenov V. V., 2018, *MNRAS*, 473, 1576
- Katushkina O. A., Alexashov D. B., Izmodenov V. V., Gvaramadze V. V., 2017, *MNRAS*, 465, 1573
- Kobulnicky H. A., Chick W. T., Povich M. S., 2018, *ApJ*, 856, 74
- Kobulnicky H. A., Chick W. T., Schurhammer D. P., Andrews J. E., Povich M. S., Munari S. A., Olivier G. M., Sorber R. L., Wernke H. N., Dale D. A., 2016, *ApJS*, 227, 18
- Kobulnicky H. A., Schurhammer D. P., Baldwin D. J., Chick W. T., Dixon D. M., Lee D., Povich M. S., 2017, *AJ*, 154, 201
- Langer N., 2012, *ARA&A*, 50, 107
- Mackey J., Gvaramadze V. V., Mohamed S., Langer N., 2015, *A&A*, 573, A10
- Mackey J., Mohamed S., Gvaramadze V. V., Kotak R., Langer N., Meyer D. M.-A., Moriya T. J., Neilson H. R., 2014, *Nature*, 512, 282
- Mackey J., Mohamed S., Neilson H. R., Langer N., Meyer D. M.-A., 2012, *ApJ*, 751, L10
- Meyer D. M.-A., Gvaramadze V. V., Langer N., Mackey J., Boumis P., Mohamed S., 2014, *MNRAS*, 439, L41
- Meyer D. M.-A., Langer N., Mackey J., Velázquez P. F., Gusdorf A., 2015, *MNRAS*, 450, 3080
- Meyer D. M.-A., Mackey J., Langer N., Gvaramadze V. V., Mignone A., Izzard R. G., Kaper L., 2014, *MNRAS*, 444, 2754
- Meyer D. M. A., Mignone A., Kuiper R., Raga A. C., Kley W., 2017, *MNRAS*, 464, 3229
- Meyer D. M.-A., van Marle A.-J., Kuiper R., Kley W., 2016, *MNRAS*, 459, 1146
- Meynet G., Maeder A., 2005, *A&A*, 429, 581
- Mignone A., Bodo G., Massaglia S., Matsakos T., Tesileanu O., Zanni C., Ferrari A., 2007, *ApJS*, 170, 228
- Mignone A., Zanni C., Tzeferacos P., van Straalen B., Colella P., Bodo G., 2012, *ApJS*, 198, 7
- Nugis T., Lamers H. J. G. L. M., 2000, *A&A*, 360, 227
- O'Hara T. B., Meixner M., Speck A. K., Ueta T., Bobrowsky M., 2003, *ApJ*, 598, 1255
- Orlando S., Bocchino F., Reale F., Peres G., Petruk O., 2007, *A&A*, 470, 927
- Osterbrock D. E., Bochkarev N. G., 1989, *Soviet Ast.*, 33, 694
- Peri C. S., Benaglia P., Brookes D. P., Stevens I. R., Isequilla N. L., 2012, *A&A*, 538, A108
- Peri C. S., Benaglia P., Isequilla N. L., 2015, *A&A*, 578, A45
- Prajapati P., Tej A., del Palacio S., Benaglia P., CH I.-C., Vig S., Mand al S., Kanti Ghosh S., 2019, *arXiv e-prints*, p. arXiv:1909.12332
- Rangelov B., Montmerle T., Federman S. R., Boisse P., Gabici S., 2019, *arXiv e-prints*, p. arXiv:1909.01424
- Reimer A., Pohl M., Reimer O., 2006, *ApJ*, 644, 1118
- Reynolds S. P., 2011, *Ap&SS*, 336, 257
- Rho J., Petre R., 1997, *ApJ*, 484, 828
- Rodríguez-González A., Meliani Z., Sánchez-Cruces M., Rivera-Ortiz P. R., Castellanos-Ramírez A., 2019, *A&A*, 631, A170
- Rozyczka M., Tenorio-Tagle G., Franco J., Bodenheimer P., 1993, *MNRAS*, 261, 674
- Sánchez-Cruces M., Rosado M., Fuentes-Carrera I., Ambrocio-Cruz P., 2018, *MNRAS*, 473, 1705
- Sanyal D., Langer N., Szcési D., -C Yoon S., Grassitelli L., 2017, *A&A*, 597, A71
- Sasaki M., Kothes R., Plucinsky P. P., Gaetz T. J., Brunt C. M., 2006, *ApJ*, 642, L149
- Schneps M. H., Haschick A. D., Wright E. L., Barrett A. H., 1981, *ApJ*, 243, 184
- Seo J., Kang H., Ryu D., 2018, *Journal of Korean Astronomical Society*, 51, 37
- Smith L. J., Pettini M., Dyson J. E., Hartquist T. W., 1984, *MNRAS*, 211, 679
- Storey M. C., Staveley-Smith L., Manchester R. N., Kesteven M. J., 1992, *A&A*, 265, 752
- Tatischeff V., Duprat J., de Séreville N., 2010, *ApJ*, 714, L26
- Telezhinsky I., Dwarkadas V. V., Pohl M., 2012a, *Astroparticle Physics*, 35, 300
- Telezhinsky I., Dwarkadas V. V., Pohl M., 2012b, *A&A*, 541, A153
- Telezhinsky I., Dwarkadas V. V., Pohl M., 2013, *A&A*, 552, A102
- Tenorio-Tagle G., Rozyczka M., Yorke H. W., 1985, *A&A*, 148, 52
- Toalá J. A., Arthur S. J., 2011, *ApJ*, 737, 100
- Toalá J. A., Guerrero M. A., 2013, *A&A*, 559, A52
- Toalá J. A., Guerrero M. A., Gruendl R. A., Chu Y. H., 2014, *AJ*, 147, 30
- Toalá J. A., Guerrero M. A., Ramos-Larios G., Guzmán V., 2015, *A&A*, 578, A66
- Toalá J. A., Oskinova L. M., González-Galán A., Guerrero M. A., Ignace R., Pohl M., 2016, *ApJ*, 821, 79
- Toalá J. A., Oskinova L. M., Ignace R., 2017, *ApJ*, 838, L19
- Toledo-Roy J. C., Esquivel A., Velázquez P. F., Reynoso E. M., 2014, *MNRAS*, 442, 229
- Truelove J. K., McKee C. F., 1999, *ApJS*, 120, 299

- van Buren D., 1993, in Cassinelli J. P., Churchwell E. B., eds, *Massive Stars: Their Lives in the Interstellar Medium* Vol. 35 of *Astronomical Society of the Pacific Conference Series, Stellar Wind Bow Shocks*. p. 315
- van Buren D., McCray R., 1988, *ApJ*, 329, L93
- van Buren D., Noriega-Crespo A., Dgani R., 1995, *AJ*, 110, 2914
- van der Hucht K. A., 2001, *New Astr. Rev.*, 45, 135
- van Marle A. J., Decin L., Meliani Z., 2014, *A&A*, 561, A152
- van Marle A. J., Keppens R., 2012, *A&A*, 547, A3
- van Marle A. J., Langer N., Achterberg A., García-Segura G., 2006, *A&A*, 460, 105
- van Marle A. J., Langer N., García-Segura G., 2007, *A&A*, 469, 941
- van Marle A. J., Meliani Z., Keppens R., Decin L., 2011, *ApJ*, 734, L26
- van Veelen B., Langer N., Vink J., García-Segura G., van Marle A. J., 2009, *A&A*, 503, 495
- Velázquez P. F., Vigh C. D., Reynoso E. M., Gómez D. O., Schneider E. M., 2006, *ApJ*, 649, 779
- Vigh C. D., Velázquez P. F., Gómez D. O., Reynoso E. M., Esquivel A., Matias Schneider E., 2011, *ApJ*, 727, 32
- Voelk H. J., Forman M., 1982, *ApJ*, 253, 188
- Wareing C. J., Pittard J. M., Falle S. A. E. G., 2017, *MNRAS*, 470, 2283
- Wareing C. J., Zijlstra A. A., O'Brien T. J., 2007, *ApJ*, 660, L129
- Weaver R., McCray R., Castor J., Shapiro P., Moore R., 1977, *ApJ*, 218, 377
- Webb G. M., Axford W. I., Forman M. A., 1985, *ApJ*, 298, 684
- Whalen D., van Veelen B., O'Shea B. W., Norman M. L., 2008, *ApJ*, 682, 49
- Wiersma R. P. C., Schaye J., Smith B. D., 2009, *MNRAS*, 393, 99
- Wilkin F. P., 1996, *ApJ*, 459, L31
- Williams B. J., Borkowski K. J., Ghavamian P., Hewitt J. W., Mao S. A., Petre R., Reynolds S. P., Blondin J. M., 2013, *ApJ*, 770, 129
- Zhekov S. A., 2014, *MNRAS*, 443, 12
- Zirakashvili V. N., Ptuskin V. S., 2018, *Astroparticle Physics*, 98, 21